Different propagation mechanisms of deep and shallow wintertime extratropical cyclones over the North Pacific

Article

Accepted Version

www.reading.ac.uk/centaur

Different Propagation Mechanisms of Deep and Shallow Wintertime Extratropical Cyclones over the North Pacific

Yuling Yao,[a] Yang Zhang,[a] Kevin I. Hodges[b,c] and Talia Tamarin-Brodsky[d]

[a] *China Meteorological Administration-Nanjing University Joint Laboratory for Climate Prediction Studies, Institute for Climate and Global Change Research, School of Atmospheric Sciences, Nanjing University, Nanjing, China*

[b] *Department of Meteorology, University of Reading, Reading, UK*

[c] *National Centre for Atmospheric Science, University of Reading, Reading, UK*

[d] *Department of Geophysics, Tel-Aviv University, Tel Aviv, Israel*

Corresponding author: Yang Zhang, yangzhang@nju.edu.cn

File generated with AMS Word template 2.0

1

ABSTRACT

Extratropical cyclones (ETCs) are three-dimensional synoptic systems in mid- and high latitudes. Previous studies on ETC propagation have typically focused on cyclones identified at a single level. However, more recent studies have found that ETCs have diverse vertical structures and cyclones with different vertical extent always exhibit distinct characteristics and surface impacts. In this work, we study the movement of wintertime (December-January-February) extratropical cyclones by classifying North Pacific ETCs into deep cyclones, shallow low-level cyclones and shallow upper-level cyclones, based on reanalysis data from 1979 to 2019. Applying a Lagrangian perspective, we track the cyclones at different vertical levels to investigate the different characteristics and mechanisms for the propagation of deep and shallow ETCs. A potential vorticity (PV) tendency analysis of cyclone-tracking composites reveals that, for deep cyclones, the diabatic heating at 850 hPa and the horizontal advection by the stationary flow at 500 hPa are the main contributors to the poleward movement. For shallow cyclones, the nonlinear advection terms play a dominant role in their meridional motion, advecting shallow low-level cyclones poleward but shallow upper-level cyclones equatorward. A piecewise PV inversion analysis suggests that the nonlinear advection by winds induced from upper-level PV anomalies is responsible for the different performance of nonlinear advection terms for shallow low-level and upper-level cyclones. These findings further our understanding of the mechanisms and variations of cyclone propagation.

SIGNIFICANCE STATEMENT

Extratropical cyclones (ETCs) can be identified at different levels in the troposphere. These mobile low-pressure cyclonic storms are the main sources of synoptic variability in the extratropics and often bring severe or even disastrous weather. Previous studies on ETC movement have typically been restricted to cyclones identified at a single level. Our study, by identifying ETCs at multiple levels, classifies cyclones into deep, shallow low-level and shallow upper-level cyclones. For deep cyclones, their poleward movement is found to be a result of diabatic heating at lower levels and dominated by the stationary circulation at upper levels. For shallow cyclones, nonlinear advection determines whether they propagate poleward or equatorward. These findings further our understanding of the mechanisms of cyclone propagation, and imply that the movement of deep and shallow cyclones may

2

File generated with AMS Word template 2.0

undergo different changes with different weather and climate impacts in the future, given the enhanced diabatic heating under global warming, which deserves further investigations.

1. Introduction

Extratropical cyclones (ETCs) are one of the fundamental synoptic systems in mid- and high latitudes. These mobile low-pressure cyclonic storms are the main sources of synoptic variability in the extratropics and often bring severe or even disastrous weather such as strong winds, cold surges, intense precipitation and snowstorms (Leckebusch and Ulbrich 2004; Pfahl and Wernli 2012; Dowdy and Catto 2017). ETCs also play a pivotal role in the poleward transport of momentum, heat, moisture, and energy (Chang et al. 2002), thus they are key components of the climate in mid- and high latitudes. Given their importance, the development and movement of ETCs has long been the focus of weather forecast and climate studies (Zhang et al. 2012; Kang et al. 2020; Kang and Son 2021).

Using Lagrangian tracking methods (Hodges 1994, 1995; Serreze 1995; Sinclair 1995, 1997; Zhang et al. 2004; Wernli and Schwierz 2006), the propagation of ETCs has been extensively studied. With reanalysis data, Blender et al. (1997) and Mendes and Mendes (2004) showed that cyclones tend to move northeastward on average in the Northern Hemisphere. Many studies have shown that the propagation of ETCs is associated with the atmospheric large-scale circulation. For example, the steering flow in front of the East Asia trough always leads to the cyclones there moving northeastward (Zhang et al. 2012); the main track direction of East Mediterranean cyclones are partly controlled by the extension of both the Azores and the Siberian highs into the East Mediterranean (Almazroui et al. 2015); the upper-level jet and the North Atlantic Oscillation (NAO) pattern, whose variations are closely coupled with the Rossby wave breaking (Woollings et al. 2008; Kunz et al. 2009), greatly influence the location and trajectory of extratropical cyclones over the North Atlantic and western Europe (Raible 2007; Gómara et al. 2014). In the Southern Hemisphere, extratropical cyclones mainly move southeastward, which can vary with the change of atmospheric circulations associated with the El Niño-Southern Oscillation (ENSO) and Southern Annual Mode (SAM) (Pezza and Ambrizzi 2003; Pezza et al. 2008).

Recently, Tamarin and Kaspi (2016, 2017a, 2017b, 2017c) adopted the potential vorticity (PV) framework, combining a PV tendency budget analysis and a piecewise PV inversion (Davis and Emanuel 1991), and diagnosed quantitatively the contributions of dynamic and

3

File generated with AMS Word template 2.0

thermodynamic processes to cyclone propagation. They pointed out the crucial role played by the upper-level PV anomaly and latent heating release (LHR) in the poleward motion of cyclones in simulations with an idealized zonal symmetric General Circulation Model (GCM) (Tamarin and Kaspi 2016), and that the stationary horizontal advection is another important factor that influences ETC propagation for cyclones simulated by an idealized GCM with a localized ocean heat flux (Tamarin and Kaspi 2017b). The above findings were all based on ETCs detected at a single tropospheric level.

However, several studies have found that ETCs have diverse vertical structures and cyclones with different vertical extents have distinct characteristics in terms of their spatial distribution and lifetime. Lim and Simmonds (2007) showed that ETCs in the Southern Hemisphere (SH) are most common at the surface and mid-troposphere, with lower occurrence frequencies observed at 700 hPa, and about 52% of SH cyclones being vertically well-organized, reaching up to 500 hPa. Pepler and Dowdy (2020) extended the analysis by investigating the global distribution of ETCs at six vertical levels. They found that about 50.4% of global cyclones can reach up to at least 500 hPa, with the percentage reaching 52% in the Northern Hemisphere (NH). Lakkis et al. (2021) explored the three-dimensional distribution of the SH extratropical cyclones and found that cyclones with different vertical extents have distinct characteristics including their spatial distribution and lifetimes. The vertical structure of an extratropical cyclone is also found to play a major role in its development and surface impacts (Flaounas et al. 2015; Pepler and Dowdy 2020). These previous studies motivate us to ask whether the vertical structure of ETCs also affects their propagation? If so, do cyclones with different vertical extents have different propagation mechanisms?

In this study, the above questions are addressed first in the wintertime North Pacific (NP) region, where ETCs occur with high frequency (Chang et al. 2002). By applying a cyclone tracking method, we identify and separate the ETCs passing through the NP region into deep, shallow low-level and shallow upper-level cyclones. To be consistent with previous studies (e.g. Pook et al. (2014); Pepler and Dowdy (2020, 2021)), we use 500 hPa vorticity to identify upper-level cyclones. We compare the propagation characteristics and investigate the propagation mechanisms of the different categories of cyclones through their PV budget and piecewise PV inversion to answer the following questions: what are the propagation characteristics of upper-, lower-level shallow cyclones and deep cyclones and what are the

4

File generated with AMS Word template 2.0

contributions of dynamic and thermodynamic processes (especially the diabatic heating) at different levels to the propagation of deep and shallow cyclones?

The rest of the paper is organized as follows. Section 2 provides a brief description of the data and methods used in the study, in which the PV tendency budget diagnostics are also introduced. In section 3, the propagation characteristics of deep and shallow cyclones are presented. In section 4, the PV budget for deep and shallow cyclones are analyzed and compared at different levels, through which different propagation mechanisms for deep and shallow cyclones are explored. Conclusions and discussions are provided in section 5.

2. Data and methods

The data utilized in this study are the 6-hourly horizontal winds, vertical velocity, geopotential, temperature and specific humidity from the European Centre for Medium-Range Weather Forecasts (ECMWF) interim Reanalysis (ERA-Interim) dataset (Dee et al. 2011) for 40 December-January-February winters, from 1979 to 2019. These variables are at a horizontal resolution of 1.5°×1.5° and 17 pressure levels. As shown in Hodges et al. (2011), the ERA-interim dataset can well represent the characteristics of ETCs. We also tested our results by using the Climate Forecast System Reanalysis (CFSR) reanalysis data from the National Centers for Environmental Prediction (NCEP) (Saha et al. 2010) at a horizontal resolution of 0.5°×0.5° and the ECMWF 5th generation reanalysis (ERA5) data (Hersbach et al. 2020) at a horizontal resolution of 0.75°×0.75°. The results are almost identical among the three different reanalysis datasets. As many of the related studies were conducted using the ERA-Interim dataset (e.g. Čampa and Wernli 2012; Seiler 2019; Pepler and Dowdy 2020; Kang and Son 2021; Lakkis et al. 2021; Jiang et al. 2022), we present the results using ERA-Interim in the main text to compare with these previous studies directly. The results using CFSR and ERA5 reanalysis data are included in the supplementary material of the manuscript.

a. Cyclone tracking and classification

As demonstrated by Raible et al. (2008) and Neu et al. (2013), though multiple cyclone tracking methods have been proposed in literature, most of them reveal consistent mean characteristics of ETCs. In this study, an automated objective feature tracking algorithm (Hodges 1994, 1995, 1999) is employed to detect and track ETCs at different tropospheric levels. This algorithm has been evaluated well and widely applied to global and regional

5

File generated with AMS Word template 2.0

cyclone tracking (Zappa et al. 2013; Seiler 2019; Kang et al. 2020; Priestley et al. 2020) in both observational (Hoskins and Hodges 2002; Chen et al. 2014) and modeling studies (Bengtsson et al. 2006; Catto et al. 2010; Côté et al. 2015). The ETCs are identified as local maxima of relative vorticity (ζ), which is calculated using the zonal and meridional velocity (u and v, respectively) as $\zeta = \dfrac{1}{R\cos\varphi}\left[\dfrac{\partial v}{\partial \lambda} - \dfrac{\partial(u\cos\varphi)}{\partial \varphi}\right]$, with λ and φ denoting the longitude and latitude, respectively, and R is the radius of Earth. The vorticity field is first smoothed to T42 to remove small-scale noise. Spatial wavenumbers smaller than 5 are also removed to eliminate the influence of the large-scale background flow and thus isolate the synoptic spatial scale variability. A threshold of 10^{-5} s^{-1} is applied to the filtered vorticity to initially identify the vorticity features on a polar stereographic projection which are then projected back to the unit sphere for tracking. The centers are tracked by first initializing a set of tracks based on a nearest-neighbor approach, these are refined by minimizing a cost function for track smoothness subject to suitable adaptive constraints for the track smoothness and displacement in a timestep (Hodges 1994, 1999). Compared with detecting cyclones from the mean sea level pressure (MSLP) or geopotential fields, utilizing the noise-preprocessed vorticity field tends to identify more small-spatial-scale systems, and makes the tracking more reliable (Hoskins and Hodges 2002; Hodges et al. 2011). In this study, only ETCs that have a lifetime longer than two days and that propagate distances greater than 1000 km are retained to focus on the more mobile systems and exclude short lived systems. With a focus on the ETCs over the NP, cyclones that originate north of 25°N and go through the target domain (30-45.5°N, 150°E-172°W) during their life cycle are kept for further analyses. The target domain is selected as the region where the track density of North Pacific ETCs reaches a maximum at both lower (850 hPa) and upper (500 hPa) levels, which is shown as the black solid box in Fig. 1. We also test our main results in a larger domain (30-50°N, 150°E-140°W; shown as the purple dashed box in Fig. 1), for which the main conclusions of the study are still hold. Therefore, our results are robust to moderate change in the domain size. The main results using the large domain are included in the supplementary material of the manuscript.

File generated with AMS Word template 2.0

a) Track Density at 850 hPa
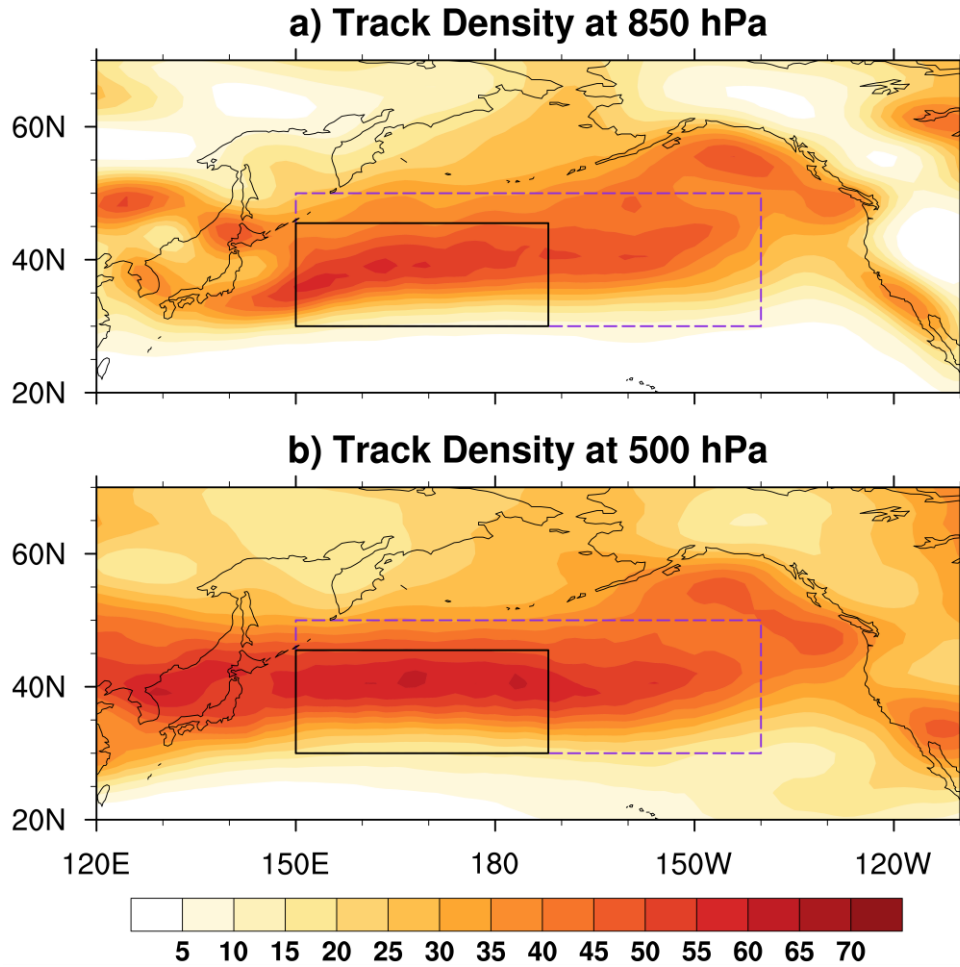

b) Track Density at 500 hPa

Fig. 1. Climatological track density over the broad North Pacific at (a) 850 hPa and (b) 500 hPa during the period from 1979 to 2018 DJF. Track density is defined as the number density per season per unit area, where the unit area is equivalent to a 5° spherical cap ($\approx 10^6$ km^2). The black solid box denotes the target domain in this study and the purple dashed box shows the larger domain used for testing the robustness of our results (see the supplementary material for more details).

As we will investigate both deep and shallow ETCs, instead of using the ζ at a single level as in most previous studies (Tamarin and Kaspi 2017a; Seiler 2019; Kang et al. 2020), the ζ at multiple levels of 850, 700, 600 and 500 hPa, i.e. $\zeta_{850\ hPa}$, $\zeta_{700\ hPa}$, $\zeta_{600\ hPa}$ and $\zeta_{500\ hPa}$, are used to detect and track cyclones. A uniform threshold of 10^{-5} s^{-1} is applied for cyclone detection at all vertical levels as in Lakkis et al. (2019) and Lakkis et al. (2021). Though as suggested in Okajima et al. (2021), the relative vorticity with the ETC always increases with height, which may have an impact on the cyclone detection, this impact can be partly reduced by our data pre-processing of the vorticity by removing the influence of the large-scale flow and the small-scale noise. Furthermore, this vertically uniform threshold is

7

File generated with AMS Word template 2.0

low enough to capture most of the cyclones at each level, which enables us to identify deep and shallow cyclones and prevents the situation in which a deep cyclone is identified as a shallow low-level cyclone by mistake due to the artificially higher threshold for cyclone detection in the upper level. Here we follow previous studies (Pook et al. 2014; Pepler and Dowdy 2020, 2021), setting 500 hPa as the level for identifying upper-level cyclones that may have surface impacts. Throughout the paper, we will discuss three categories of ETCs, as defined in the schematic diagram shown in Figure 2. For an ETC, if its local maximum relative vorticity is detected at each of the above four pressure levels from 850 hPa to 500 hPa within a 5° circle at the same timestep, the ETC is classified as a deep cyclone. By contrast, if an ETC is detected at 850 hPa but not extending up to 500 hPa, the ETC is classified as a shallow low-level cyclone. Similarly, if an ETC's vorticity center is found at 500 hPa but not extending down to 850 hPa, the ETC is defined as a shallow upper-level cyclone. Note that in order to avoid any overlap between deep and shallow cyclones, only the parts of a cyclone track where cyclones are detected at all levels are considered as "deep" cyclones in our study. Similarly, for the other non-deep cyclone tracks, only the parts of a cyclone track where cyclones are identified within the upper or lower levels are considered as "shallow" cyclones. In addition, an extra threshold for the duration of deep and shallow cyclones is applied to guarantee that typical deep or shallow systems are used for composite, which is introduced in detail in Section 2b.

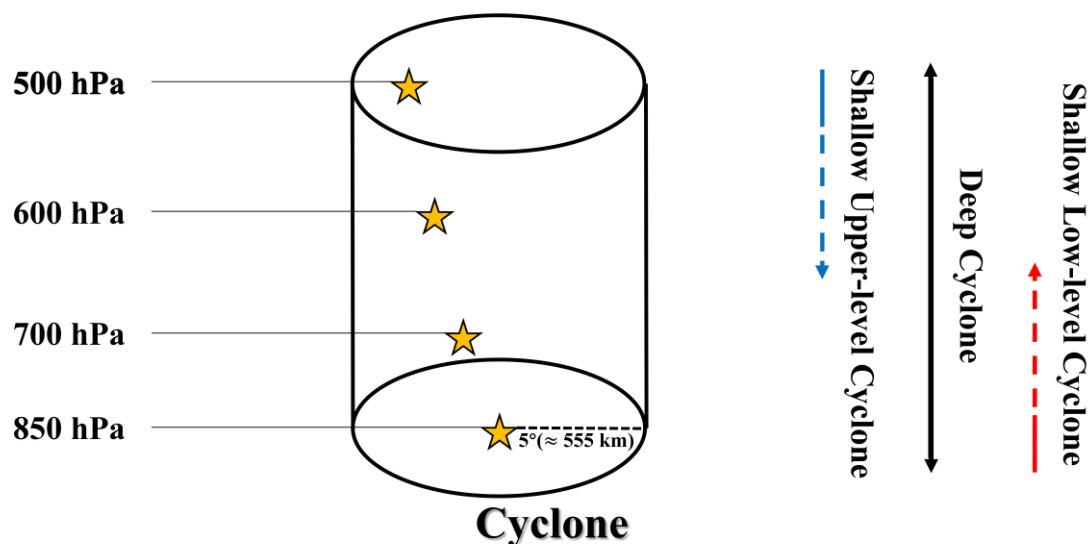Fig. 2. Schematic showing the levels included for each category of cyclones. Stars indicate the location of the maximum relative vorticity at each level. The cylinder with a radius of 5° (≈ 555 km) shows the searching range. On the right, the vertical extents of deep cyclone, shallow upper- and low-level cyclone are displayed. The solid lines denote levels

8

File generated with AMS Word template 2.0

where cyclones can be detected, and dashed lines denote optional levels where cyclones may reach or not.

b. Cyclone composites

The tracking data are employed to construct composites of cyclones in a similar manner to Tamarin and Kaspi (2016). For each cyclone, a box of size 30 degrees in both latitude and longitude is placed around its center at every time step. Fields of interest, with the same horizontal resolution as the original data, are sampled along the trajectory and then averaged over all tracks at selected lifecycle stages.

To concentrate on the developing cyclones in the NP, only the timesteps during which the ETC passes through the target region during its growth stage are composited. Moreover, to avoid the situation where local vorticity maxima at different levels occasionally occur at the same time in the nearby region but do not belong to the same cyclone system, an additional duration threshold is applied to the timesteps used for the composite analysis. For deep cyclones, the trajectories lasting for at least 24 hours in the target region are kept for the composite. For the shallow cyclones, the requirement for the minimum duration of the trajectory in the target region is reduced to 12 hours as shallow cyclones always have a shorter lifetime compared with deep cyclones (Lim and Simmonds 2007; Pepler and Dowdy 2020). In total, there are 215 deep cyclones, 115 shallow low-level cyclones, and 110 shallow upper-level cyclones used for the composite analysis. We have tested our results by investigating ETCs over the larger domain of the NP, in which more cyclones are used for the composite. The results are almost identical, except that the stationary flow may play a more important role in the background flow, and our conclusions still hold for such a change in domain size (see supplementary material for more details). We have also tested our results by setting a no duration threshold or a stricter duration threshold on the timesteps during which the cyclone passes the target NP region. Though the selection of the duration threshold alters the number of cyclones for the composites, it does not qualitatively change the main results of our analysis (results not shown).

c. PV tendency budget

As shown in many previous studies (Tamarin and Kaspi 2016; Kang and Son 2021), the development and propagation of ETCs can be well represented by PV, which makes it relatively simple to combine the dynamic and thermodynamic influence. In this study we use

9

File generated with AMS Word template 2.0

the three-dimensional Ertel PV to investigate the development and propagation of ETCs. Its expression in pressure coordinates is given as:

$$q = -g\left[-\frac{\partial v}{\partial p}\mathbf{i} + \frac{\partial u}{\partial p}\mathbf{j} + \left(f + \frac{\partial v}{\partial x} - \frac{\partial u}{\partial y} \right)\mathbf{k} \right] \cdot \nabla\theta , \tag{1}$$

where $\mathbf{i}$, $\mathbf{j}$, $\mathbf{k}$ are the unit vectors along the x, y, p axis, respectively, $\nabla = \left(\partial/\partial x, \partial/\partial y, \partial/\partial p \right)$ is the three-dimensional gradient operator in pressure coordinates, g is the gravitational acceleration, f is the planetary vorticity and θ is the potential temperature. Note that the horizontal derivatives are calculated on a sphere (i.e., $\partial/\partial x = \partial/R\cos\varphi\partial\lambda$, $\partial/\partial y = \partial/R\partial\varphi$, where λ and φ are the longitude and latitude, respectively, and R is the radius of Earth). Its tendency equation is:

$$\frac{dq}{dt} = Q + F . \tag{2}$$

Here $d/dt = \partial/\partial t + u\,\partial/\partial x + v\,\partial/\partial y + \omega\,\partial/\partial p$ is the material derivative. The partial differentials for both time and space on the right-hand side (RHS) are approximated using a centered finite difference, and ω is the vertical velocity. The friction term $\left(F \right)$ and the diabatic heating term $\left(Q \right)$ are all nonconservative processes. The latter is estimated as follows (Tamarin and Kaspi 2016):

$$Q = -g\left[-\frac{\partial v}{\partial p}\mathbf{i} + \frac{\partial u}{\partial p}\mathbf{j} + \left(f + \frac{\partial v}{\partial x} - \frac{\partial u}{\partial y} \right)\mathbf{k} \right] \cdot \nabla\left(\frac{d\theta}{dt} \right). \tag{3}$$

In this study, the diabatic heating Q is split into two parts: the first is the diabatic heating due to the release of latent heating, denoted as Q_{LHR}; the remainder of the diabatic heating, such as radiation, is all included in Q_{RES}. The Q_{LHR} is calculated by replacing the $\left(d\theta/dt \right)$ in Eq. (3) with the rate of latent heating $\left(d\theta/dt \right)_{LHR}$, which is evaluated using the expression derived by Emanuel et al. (1987),

$$\left(\frac{d\theta}{dt} \right)_{LHR} = \omega\left(\frac{\partial\theta}{\partial p} - \frac{\gamma_m}{\gamma_d}\frac{\theta}{\theta_E}\frac{\partial\theta_E}{\partial p} \right), \tag{4}$$

where γ_m and γ_d stand for the moist and dry adiabatic lapse rates, respectively. The equivalent potential temperature θ_E is calculated using the formulas in Bolton (1980, Equations 16, 21, 24 and 39), which is supposed to be the most accurate non-iterative formulation available according to Davies-Jones (2009). In the formulas, θ_E is calculated from the lifting condensation level.

To diagnose the contributions of atmospheric flows with different spatial and temporal scales to the cyclone propagation, we follow Tamarin and Kaspi (2017b) and decompose the zonal flow as $u(x, y, p, t) = [\bar{u}](y, p) + \bar{u}^*(x, y, p) + u'(x, y, p, t)$, with an overbar denoting time mean, square brackets denoting zonal mean, a prime denoting transient component (deviation from the winter average in each year), and the asterisk denoting the deviation from zonal mean. Accordingly, the time-mean zonal background flow ($\bar{u}$) consists of two components: the time- and zonal-mean zonal background flow $[\bar{u}]$, which is zonally symmetric; and the time-mean and zonal asymmetric background flow $\bar{u}^*$, the stationary zonal velocity. The background states in the North Pacific are distinctively zonally-nonuniform thus the stationary circulation such as the Aleutian low dominates the time-mean background flow. The meridional flow is decomposed as $v(x, y, p, t) = \bar{v}^*(x, y, p) + v'(x, y, p, t)$, in which the time- and zonal-mean meridional background flow $[\bar{v}]$ is small in magnitude and therefore neglected. Similarly, the PV is decomposed as $q(x, y, p, t) = [\bar{q}](y, p) + \bar{q}^*(x, y, p) + q'(x, y, p, t)$, in which only the transient PV (q') varies with time. Accordingly, Eq. (2) can be re-written as

$$\frac{\partial q}{\partial t} = \left(\underbrace{-[\bar{u}]\frac{\partial q'}{\partial x}}_{\substack{\text{Advection of the} \\ \text{transient PV} \\ \text{perturbation by} \\ \text{the time- and} \\ \text{zonal-mean} \\ \text{background flow}}} \underbrace{-\bar{u}^*\frac{\partial q'}{\partial x} -\bar{v}^*\frac{\partial q'}{\partial y}}_{\substack{\text{Advection of the} \\ \text{transient PV} \\ \text{perturbation by the} \\ \text{stationary velocity}}} \underbrace{-u'\frac{\partial q'}{\partial x} -v'\frac{\partial q'}{\partial y}}_{\substack{\text{Sum of the} \\ \text{nonlinear} \\ \text{advection}}} \underbrace{-v'\frac{\partial [\bar{q}]}{\partial y} -\bar{v}^*\frac{\partial [\bar{q}]}{\partial y}}_{\substack{\text{Advection of the time-} \\ \text{and zonal-mean} \\ \text{background PV by the} \\ \text{meridional velocity}}} \right. \tag{5}$$

$$\left. -[\bar{u}]\frac{\partial \bar{q}^*}{\partial x} -u'\frac{\partial \bar{q}^*}{\partial x} -\bar{u}^*\frac{\partial \bar{q}^*}{\partial x} -v'\frac{\partial \bar{q}^*}{\partial y} -\bar{v}^*\frac{\partial \bar{q}^*}{\partial y} \right) -\omega\frac{\partial q}{\partial p} +Q_{LHR} +F_{RES}.$$

File generated with AMS Word template 2.0

$$\underbrace{\hspace{5cm}}$$

Advection of the stationary PV perturbation by the horizontal velocity

Note that the tendency of total PV on the left-hand side is essentially the tendency of the transient PV (i.e. $\partial q/\partial t = \partial q'/\partial t$). The terms in the brackets on the RHS of Eq. (5) represent the PV tendency due to the horizontal advection by different-scale flows, including the advection of the transient PV perturbation by the time- and zonal-mean background flow, sum of the advection of the transient PV perturbation by the zonal and meridional stationary velocities, sum of the nonlinear advection terms associated with the transient perturbation itself, the advection of the time- and zonal-mean background PV by the meridional velocity and the advection of the stationary PV perturbation by the zonal and meridional winds. The term $-\omega\,\partial q/\partial p$ denotes the PV tendency from vertical advection and Q_{LHR} denotes the PV tendency due to the diabatic processes associated with LHR. The last term F_{RES}, which is the sum of Q_{RES} and F, is not the focus of this study and thus is not explicitly treated and quantified.

3. The propagation characteristics of cyclones over the North Pacific

a. The climatology of cyclone propagation characteristics at different pressure levels

Before comparing the propagation characteristics of deep and shallow cyclones, we first check the climatological track, genesis and lysis density of all ETCs that originate poleward of 25°N and pass through the NP domain during their lifetime. These statistics are defined and estimated using the same methods as in Hodges (1996) and Hoskins and Hodges (2002). The track density is defined as the number of cyclone systems passing through a region. The genesis and lysis density are computed as a probability density function (PDF), with the former denoting the density of where cyclone systems originate thus computed using the starting points of tracks, and the latter denoting the density of where cyclone systems disappear thus computed using all the end points of the tracks. All of the three densities are scaled to number densities per season with a unit area equivalent to a 5° spherical cap ($\approx 10^6$ km^2) for analysis and display.

Figures 3a and 3b compare the track density of cyclones at 850 hPa and 500 hPa, respectively. Note that Figure 3 displays the distribution of all wintertime extratropical cyclones passing through the NP domain during their lifetime. As expected, the track density

12

File generated with AMS Word template 2.0

reaches a maximum at both levels within the target region (the black box in Fig. 3a). However, the spatial distribution of track density at 850 hPa shows an evident southwest-northeast (SW-NE) tilt (Fig. 3a), while at 500 hPa it crosses the NP zonally with a slightly poleward shift downstream of the box (Fig. 3b). The genesis density of cyclones at 850 hPa in Figure 3c exhibit a maximum near the east coast of Japan and in the central Pacific where the track density also reaches a maximum. At 500 hPa, the genesis density is most pronounced within the target domain (Fig. 3d), and lies at higher latitudes and more downstream than that at 850 hPa. The distributions of the track density and genesis density suggest that the SW-NE distribution of ETC track density in lower levels, especially west of 160°E, is likely due to the frequent passage of ETCs along the Kuroshio and its extension (Schemm et al. 2021; Kuwano-Yoshida et al. 2022), in which the oceanic frontal zone intensifies cyclogenesis and strengthens the North Pacific storm-track as suggested by Kelly et al. (2010) and Ma et al. (2017). Lysis, as shown in Figures 3e and 3f, mainly occurs over the ocean with a strong maximum over the Gulf of Alaska at both 850 and 500 hPa, with the lysis regions reaching higher latitudes at 850 hPa. The spatial distributions of the above three densities all suggest that the cyclones at 850 hPa tend to propagate more poleward than those at 500 hPa.

We now focus on the propagation characteristics of the above ETCs during their growth stage, which is the period during which the intensity of an ETC grows to its maximum. Table 1 lists the mean genesis latitude, the mean latitude where cyclone intensity (measured by the vorticity at the cyclone center) reaches a maximum, and the mean latitudinal displacement of cyclones (calculated as the difference of the first two latitudes) at different levels, which shows the propagation direction of cyclones more directly. It can be seen that the average genesis latitude of NP cyclones tends to increase with height, whereas the mean latitude of the cyclone peak intensity shows the opposite trend. The latitudinal displacement is positive at lower levels, which implies that cyclones generally move northward until they reach their maximum intensity, consistent with Tamarin and Kaspi (2016). However, the latitudinal displacement decreases with height and even turns to negative values at upper levels (i.e. -1.2479° at 600 hPa, -3.6545° at 500 hPa), which means that cyclones propagate southward on average. The different latitudinal displacements of cyclones at different levels suggest the possibility that deep and shallow cyclones may have different propagation characteristics, which will be further explored in Section 3b.
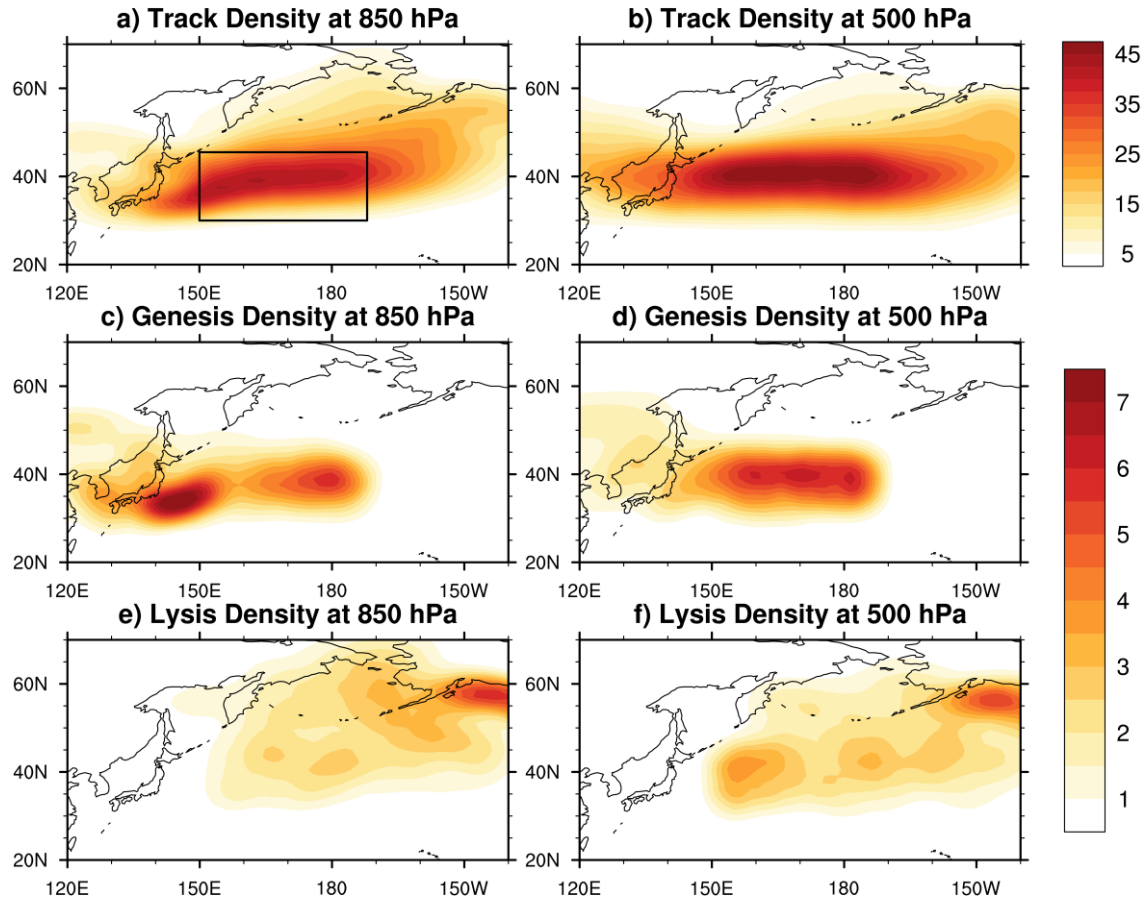
13

Fig. 3. Climatological track density (a, b), genesis density (c, d), lysis density (e, f) of cyclones that generate poleward of 25°N and pass through the target domain (30-45.5°N, 150°E-172°W; shown as the black box in panel a) during their lifetime at 850 hPa (left column) and 500 hPa (right column), respectively. All densities are defined as number densities per season per unit area, where the unit area is equivalent to a 5° spherical cap ($\approx 10^6 \, km^2$).

Pressure levels	850 hPa	700 hPa	600 hPa	500 hPa
Genesis latitude (degree)	38.2428	40.6866	43.0192	43.7717
Max. intensity latitude (degree)	44.7696	43.5141	41.7480	40.1089
Latitudinal displacement (degree)	6.5268	2.8275	-1.2712	-3.6628

Table 1. The mean genesis latitude, the mean latitude where cyclone intensity reaches maximum and the mean latitudinal displacement of cyclones (difference of the first two latitudes) over the North Pacific, shown for the four levels used in this study.

14

b. The propagation characteristics of deep and shallow cyclones

To illustrate the propagation characteristics of deep and shallow cyclones, the average trajectories of deep cyclones, shallow low-level cyclones and shallow upper-level cyclones are calculated and displayed in Figure 4. The average trajectories for each cyclone category are obtained by interpolating all of the cyclone tracks that will be used for the composite onto the same length using an interpolation method (Kim et al. 2011) and then averaging. It is shown that, for deep cyclones (as shown in solid lines), the cyclone center at each of the pressure levels moves eastward consistently, with a slight poleward shift. For shallow low-level cyclones (as shown in the red dashed line), they move poleward, more than the deep cyclones, as they move eastward. The shallow upper-level cyclones (as shown in the blue dashed line) move eastward and slightly equatorward, in contrast to the poleward movement of the deep cyclones at 500 hPa (as shown in the blue solid line). We also investigate the composite results of cyclone track statistics for deep and shallow cyclones at 850 hPa and 500 hPa in supplemental material (Figure S14), which further shows the differences in their track spread within the target domain for the three categories of cyclones. These results clearly demonstrate that deep and shallow cyclones exhibit distinct propagation characteristics, whose underlying mechanisms will be further investigated in Section 4.
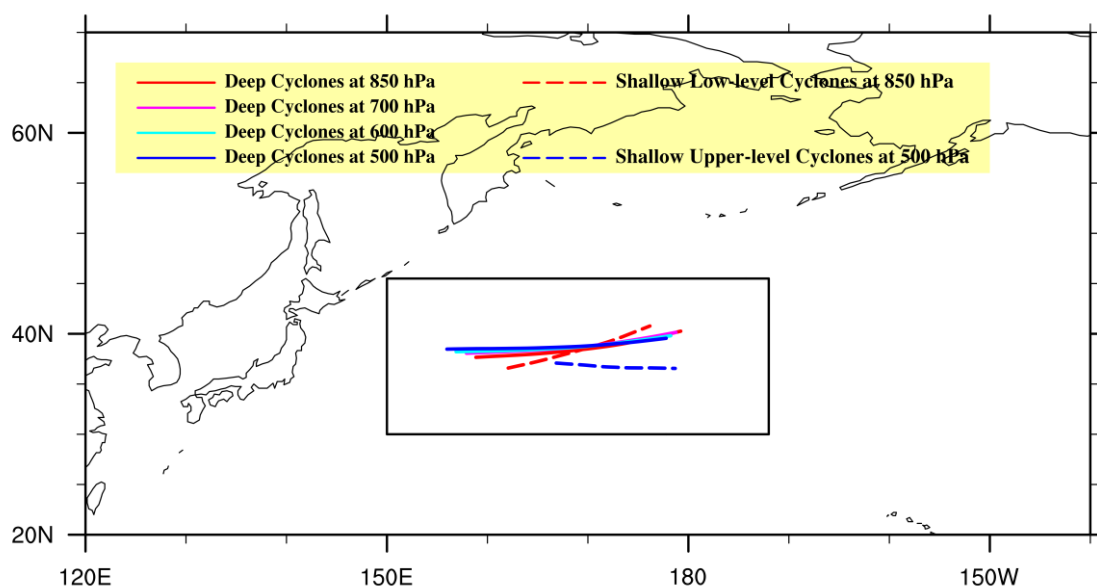

Fig. 4. Mean trajectories of deep cyclones, shallow low- and upper- level cyclones (as defined in Fig. 2). Note that only the parts of the track within the target domain (black box) are kept for analysis. The solid lines are for deep cyclones, with different colors denoting the tracks of counterparts at different levels (red: 850 hPa; pink: 700 hPa; light blue: 600 hPa; blue: 500 hPa). The trajectories of shallow low-level cyclones at 850 hPa and shallow upper-level cyclones at 500 hPa are shown by the red and blue dashed line, respectively.

15

File generated with AMS Word template 2.0

4. PV tendency budget analysis

In order to confirm the representativeness of the cyclones used for the composites, we first examine the composite of the three-dimensional distribution of the transient PV perturbation, q', (PV anomaly, in short hereafter) for deep, shallow low-level and shallow upper-level cyclones (Fig. 5). As shown in Figure 5a, for deep cyclones, strong positive PV anomalies are observed throughout the troposphere, with local maxima at 850 hPa and in the upper troposphere. Above 600 hPa, the strength of the PV anomaly increases with height, with the area of strong PV anomaly spanning about 20° zonally in the upper troposphere. For the shallow low-level cyclones (whose mean trajectory at 850 hPa is denoted by the red dashed line in Fig. 4), the positive PV anomaly is confined below 700 hPa and a negative anomaly is present above it (Fig. 5b). For the shallow upper-level cyclones (whose mean trajectory at 500 hPa is denoted by the blue dashed line in Fig. 4), the associated strong PV anomaly is confined in the upper levels (Fig. 5c). The configuration of deep and shallow upper-level cyclones are similar to that of deep and shallow cut-off lows in Barnes et al. (2021), and that of strongest and average cut-off lows in Pinheiro et al. (2021). We also display the three-dimensional structures of the relative vorticity, geopotential height, horizontal winds and temperature anomalies in Figure S15-18 in the supplemental material. The results are consistent with the three-dimensional structure the PV anomalies here. The three-dimensional composite slices all demonstrate that the three different categories of cyclones have distinct vertical structures, whose PV tendency budget will be explored next to understand their propagation mechanisms.

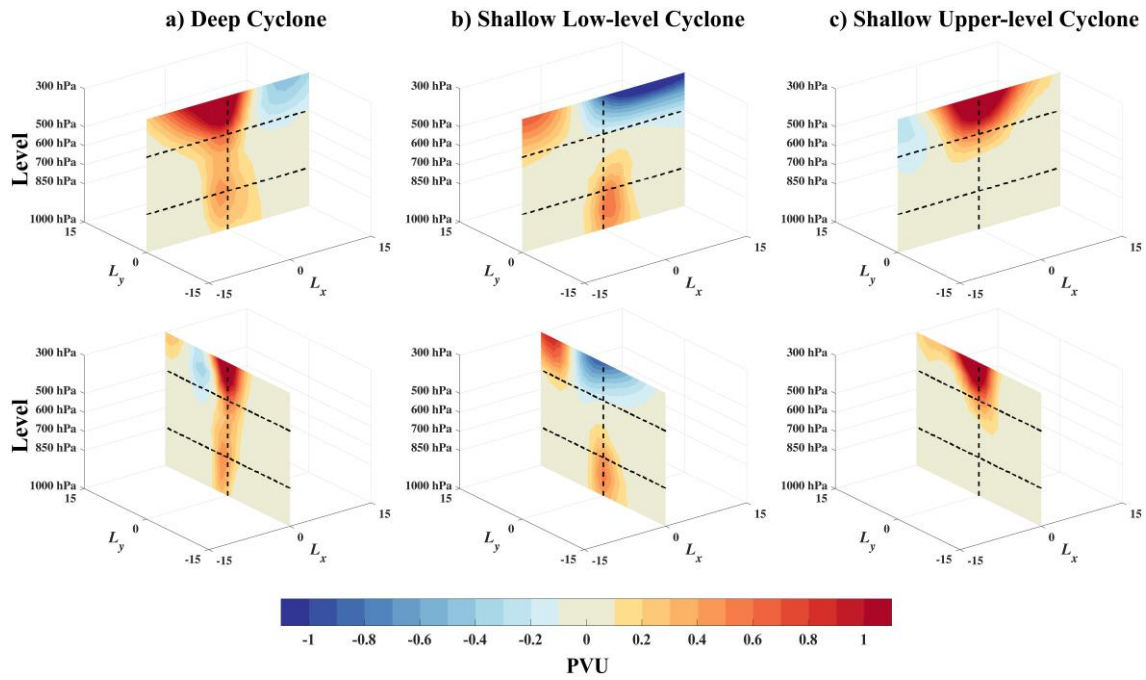**a) Deep Cyclone** **b) Shallow Low-level Cyclone** **c) Shallow Upper-level Cyclone**

Fig. 5. The zonal- (top row) and meridional- (bottom row) vertical cross sections of the transient PV perturbation (PV anomaly, unit: PVU) composites for (a) deep cyclones, (b) shallow low-level cyclones and (c) shallow upper-level cyclones. The black horizontal dashed lines indicate the 850 hPa and 500 hPa and the black vertical dashed line indicates the central axis of the cyclone. Lx and Ly denote the longitude and latitude extent of the composite box, respectively.

a. Horizontal advection terms and piecewise PV inversion

1) THE ROLE OF HORIZONTAL ADVECTION TERMS AT 850 HPA

We begin by investigating the role of the low-level horizontal advection in the propagation of deep and shallow low-level cyclones. A full decomposition of the horizontal advection term in the PV budget is given in Eq. (5), which includes the advection of the transient PV perturbation by the time- and zonal-mean flow, the stationary flow and the transient flow, the advection of the time- and zonal-mean background PV and the advection of the stationary PV perturbation. We calculated each of the above advection terms at 850 hPa. The first five terms in Eq. (5) are plotted in Figures 6 and 7 for deep and shallow low-level cyclones, respectively. The results of the other terms are not shown due to their smaller magnitude or little contribution to the propagation of the two categories of cyclones.

For deep cyclones, the instantaneous PV tendency $\left(\partial q / \partial t \right)$ shown in Figure 6a has a SW-NE tilted dipolar structure, indicating a tendency for the northeastward propagation of

17

File generated with AMS Word template 2.0

cyclones. The advection of the PV anomaly by the time- and zonal-mean background flow, as shown in Figure 6b, exhibit a zonal dipolar structure, suggesting a tendency of eastward movement of cyclones, which is primarily due to the advection of the time- and zonal-mean westerly flow. The advection by the stationary flow (Fig. 6c) shows a similar zonal dipolar structure as in Figure 6b, which is primarily due to the westerly stationary flow at the center of the cyclones. The sum of the nonlinear terms $\left(-u'\,\partial q'/\partial x - v'\,\partial q'/\partial y\right)$, as shown in Figure 6d, exhibits a significant negative tendency at the eastern side of the PV anomaly, counteracting the eastward propagation of cyclones. Positive tendencies exist at both the northwestern and southwestern sides of the cyclones, but have no clear contribution to the cyclones' poleward movement due to their symmetric position and comparable magnitude. As a result, this term mainly acts to hinder the movement of cyclones. We further decompose the nonlinear advection term into contributions from the zonal and meridional nonlinear advection. As shown in Figures 6e and 6f, each of them is characterized by a quadrupole structure with the former almost dominating their sum. Overall, the horizontal advection terms at 850 hPa are responsible for the eastward propagation of deep cyclones but have no net contribution to the poleward movement.
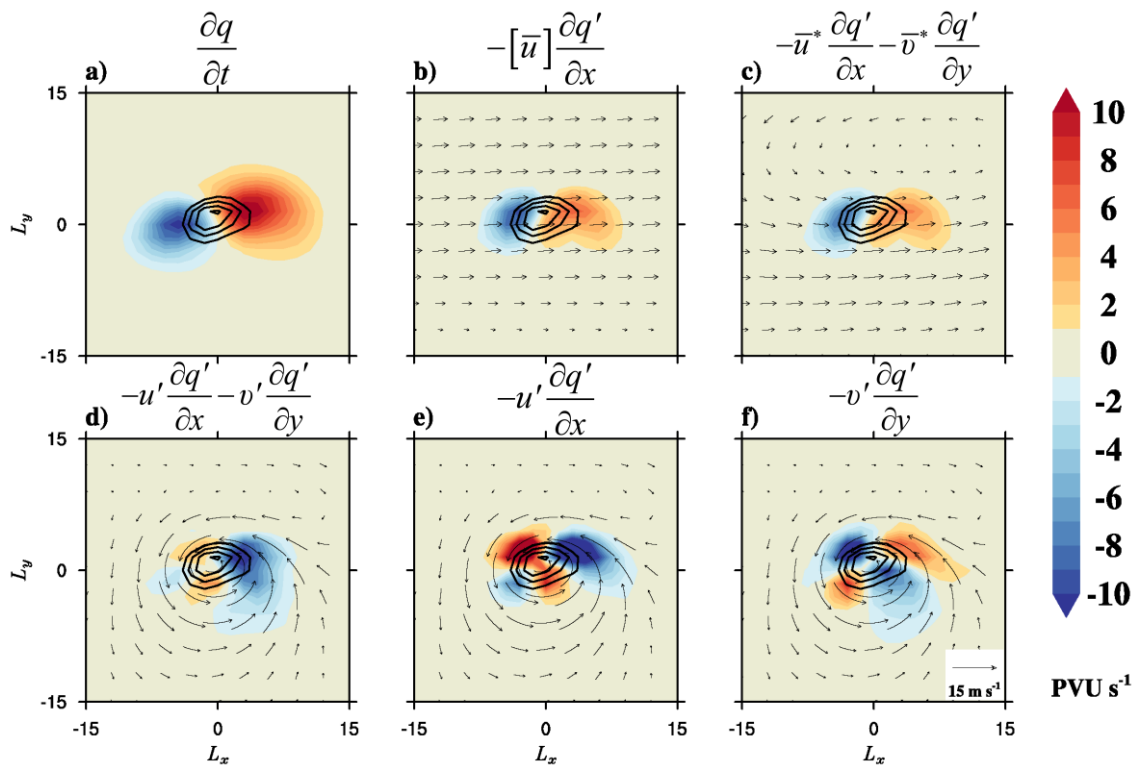

18

File generated with AMS Word template 2.0

Fig. 6. Composites of 850 hPa PV tendencies for deep cyclones: (a) instantaneous $\partial q/\partial t$, (b)-(d) is the horizontal advection of the transient PV perturbation by (b) the time- and zonal-mean velocity, (c) the stationary velocity, (d) the transient velocity (also denoted as the sum of nonlinear advection terms), (e) nonlinear zonal advection and (f) nonlinear meridional advection. All quantities are normalized by 10^{-6} PVU s^{-1}. The black arrows in panel (b) denote the direction of time- and zonal-mean wind, in panel (c) denote the direction of stationary winds, and denote the direction of transient velocities at 850 hPa in panels (d)-(f). The black arrow in the corner of panel (f) indicates a reference wind vector. In all panels, the 850 hPa transient PV perturbation is plotted in black contours, with contour interval of 0.1 PVU (contours are plotted from 0.2 PVU). Lx and Ly denote the longitude and latitude extent of the composite box, respectively.

For shallow low-level cyclones, the instantaneous PV tendency (Fig. 7a) also exhibits a dipolar structure but with a more poleward tilt in the SW-NE direction, suggesting a more poleward deflection during its propagation. The advection of the PV anomaly by the time- and zonal-mean background flow (Fig. 7b) and the stationary flow (Fig. 7c) at 850 hPa also show a zonal dipolar pattern, similar to that of deep cyclones, that merely contribute to the eastward movement of the cyclones. However, the nonlinear advection terms for the low-level shallow cyclones (Figs. 7d-f), exhibit a completely different pattern from that of the deep cyclones. The sum of nonlinear terms (Fig. 7d) produces a north-south dipolar structure, suggesting a tendency for poleward propagation. The nonlinear term is dominated by the nonlinear advection by the meridional wind (Fig. 7f). The zonal nonlinear advection term (Fig. 7e) is also characterized by a north-south dipolar structure but with opposite signs and weaker amplitudes, and thus offsets part of the tendency for poleward movement. Compared with deep cyclones, the horizontal advection terms at 850 hPa of shallow cyclones not only contribute to the eastward propagation, but also play a significant role in their poleward movement.

19
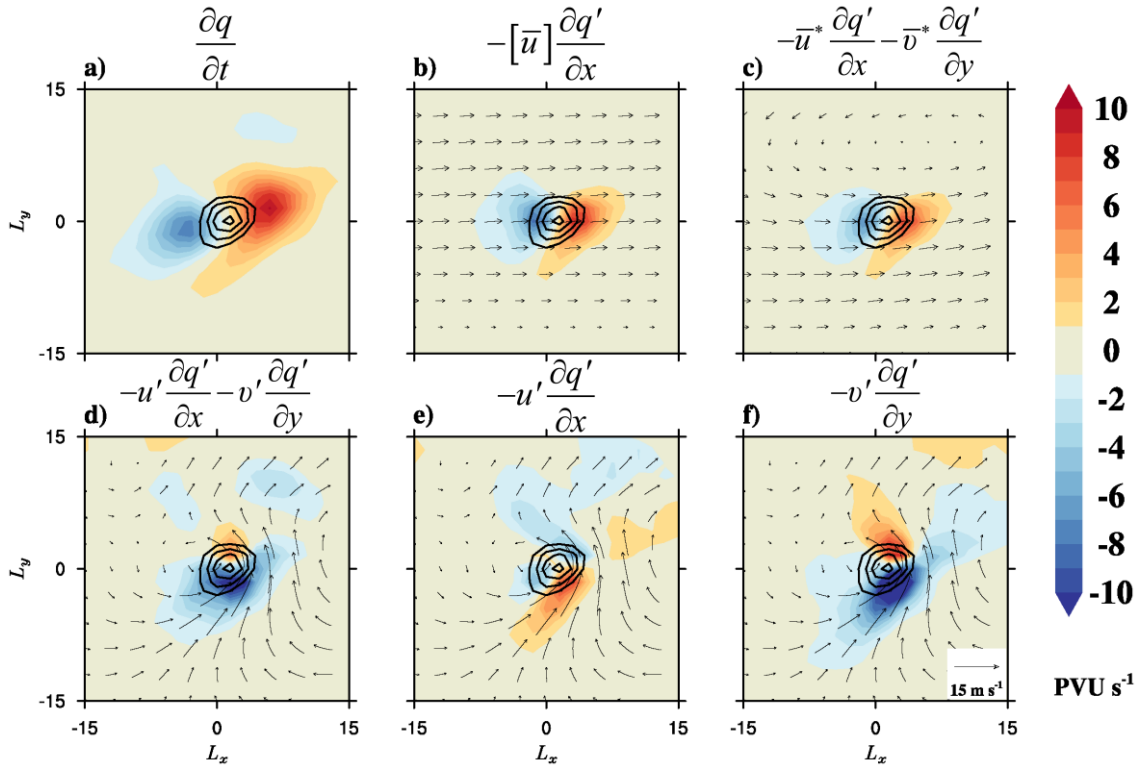
File generated with AMS Word template 2.0

Fig. 7. Same as Fig. 6, but for shallow low-level cyclones.

The above analysis shows that the nonlinear advection term plays a completely different role in the propagation of deep and shallow cyclones at 850 hPa, which may be crucial for understanding their different propagation mechanisms. To study the origin for the different effects of the nonlinear advection term between deep and shallow cyclones, we further employ a piecewise PV inversion (PVI) technique (Davis and Emanuel 1991; Davis 1992) to decompose the horizontal velocity at 850 hPa. The piecewise PV inversion (Davis 1992) allows one to decompose the PV anomaly into several significant parts, and the contribution of each part of the PV anomalies to the winds at a particular atmospheric level of interest can be studied separately. The algorithm employs the nonlinear balanced equation of Charney (1955), which is solved using a standard successive overrelaxation technique (Davis and Emanuel 1991; Davis 1992). Each piecewise inversion is achieved by setting the other parts of the PV anomalies to zero and using homogeneous lateral boundary conditions. The inversion procedure returns the three-dimensional streamfunction and geopotential height for each PV anomaly, and the associated winds can be derived at any level of interest. The piecewise PV inversion allows us to decompose the nonlinear advection term into contributions from PV anomalies at different vertical levels and to distinguish the influence

20

File generated with AMS Word template 2.0

of each of them. A composite analysis of the piecewise inversion is done as follows: for each cyclone from a specific category, we perform a piecewise PV inversion in a box around its center at each timestep, and then average all timesteps and all cyclones.

For deep cyclones, the different contributions of the PV anomalies at different levels to the horizontal nonlinear advection term at 850 hPa are shown in Figure 8, in which the contributions of the PV anomaly around 850 hPa itself $\left(PV'_{850-700\ hPa}\right)$, and the PV anomalies below $\left(PV'_{1000-925\ hPa}\right)$ and above $\left(PV'_{600-250\ hPa}\right)$ 850 hPa are investigated. The nonlinear advection terms induced from the $PV'_{1000-925\ hPa}$ are shown in Figures 8a-c. The nonlinear advection induced by the low-level PV anomaly shows a north-south dipolar structure (Fig.8a), which acts to push the cyclone southward. Its zonal and meridional components in Figures 8b-c show that the meridional nonlinear PV advection, with a north-south dipolar structure dominates the total nonlinear advection term. The zonal and meridional nonlinear advection by the winds induced from the $PV'_{850-700\ hPa}$, associated with the cyclone itself, shows a relatively symmetric quadrupole structure with opposite signs (Figs. 8e and 8f). Therefore, they mainly offset each other, and their sum (Fig. 8d) has little contribution to the propagation of the deep cyclones at 850 hPa. Figures 8g-i show the nonlinear PV advection associated with the $PV'_{600-250\ hPa}$. The zonal nonlinear advection (Fig. 8h) mainly acts to advect the cyclone westward. The meridional nonlinear advection (Fig. 8i) exhibits a meridional dipolar structure that is opposite to that from the $PV'_{1000-925\ hPa}$, acting to advect the cyclone northward. The meridional nonlinear advection again dominates the sum of the two (Fig. 8g). Compared with the original term in Fig. 6d, the total nonlinear advection (Fig. 8j) recovered from the sum of PV anomaly pieces shows stronger positive anomalies on the northern side of the cyclone center, which is primarily because the v anomaly induced from the piecewise PV inversion is slightly stronger there (not shown). Though the quadrupole structures of zonal and meridional nonlinear advection terms (Fig. 8k and Fig. 8l) are well re-produced, they have opposite patterns and mostly cancel each other, which emphasizes the difference. Even though, the nonlinear advection has little effect on the meridional movement of the cyclone. Although the nonlinear advection by winds induced from the $PV'_{600-250\ hPa}$

21

acts to advect the cyclone poleward, it is greatly offset by the equatorward advection by

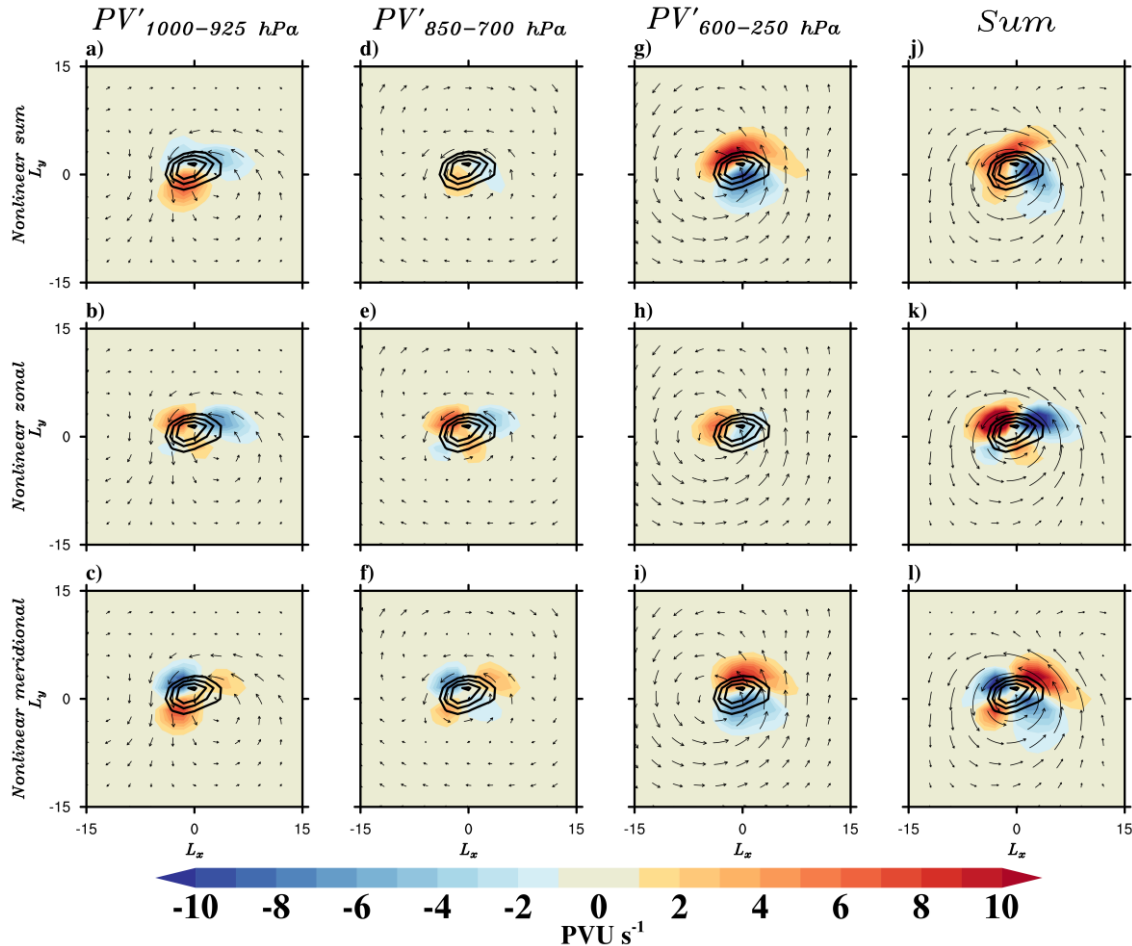winds induced from the $PV'_{1000-925\ hPa}$.

Fig. 8. Piecewise PV decomposition of the nonlinear PV advection term for deep cyclones. Contributions to the PV tendency at 850 hPa from (top)-(bottom) the sum of nonlinear advection terms, the zonal and meridional nonlinear advection. (left)-(right) The contributions to nonlinear PV advection at 850 hPa induced from the PV anomaly at 1000-925 hPa, 850-700 hPa, 600-250 hPa and the sum. All quantities are normalized by 10^{-6} PVU s^{-1}. In each panel the associated winds (black arrows) induced by each of the PV pieces above are also shown, and the reference wind vector (not shown here) is the same as that in Fig. 6. In all panels, the 850 hPa PV anomaly is plotted in black contours, with contour interval of 0.1 PVU (contours are plotted from 0.2 PVU). L_x and L_y denote the relative longitude and latitude extent of the composite box, respectively.

For shallow low-level cyclones, the results of the piecewise PV inversion are shown in

Figure 9. Although there are some differences between the overall sum (Fig. 9j) and the

original term (Fig. 7d) on the northern side of the cyclone center, the typical dipolar

22

File generated with AMS Word template 2.0

structures are still reproduced, indicating that the nonlinear advection does contribute to the poleward movement of cyclones. As shown in Figures 9a, 9d and 9g, only the nonlinear advection from the $PV'_{600-250\ hPa}$ (Fig. 9g) exhibits a north-south dipolar structure, and thus it plays a major role in the poleward tendency of the 850 hPa PV anomaly, which is dominated by its meridional component (Fig. 9i). Although the meridional nonlinear advection from the $PV'_{1000-925\ hPa}$ (Fig. 9c) also produces a positive and negative PV tendency on the northern and southern sides of the PV anomaly, respectively, the tendency of poleward movement is greatly offset by the zonal nonlinear advection (Fig. 9b). Consequently, their sum mainly shows a west-east dipolar structure on the northern side of the cyclone (Fig. 9a), and thus has little contribution to the poleward propagation of cyclones. Through the piecewise PV inversion analysis, it is concluded that different from deep cyclones, the nonlinear advection by winds induced from the $PV'_{600-250\ hPa}$ plays a major role in the poleward movement of cyclones.

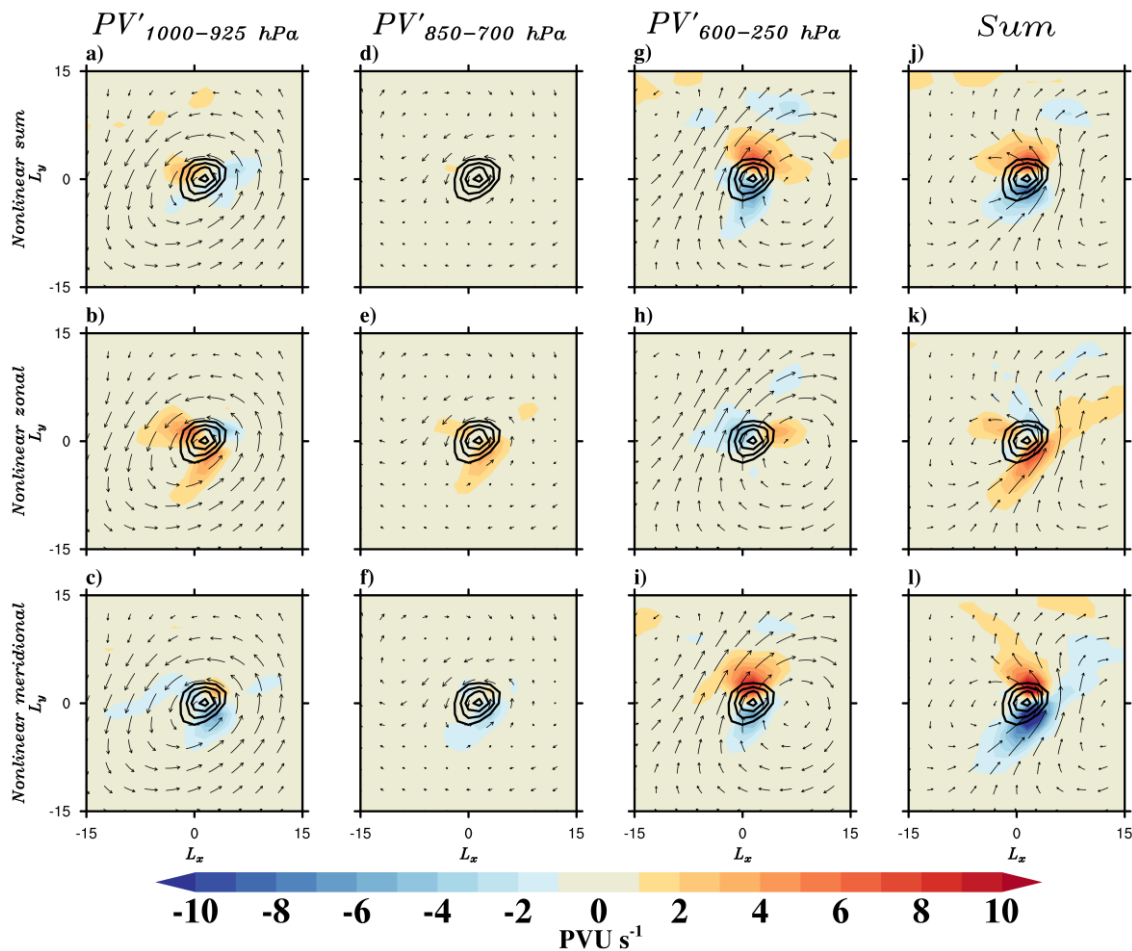Fig. 9. Same as Fig. 8, but for shallow low-level cyclones.

File generated with AMS Word template 2.0

2) THE ROLE OF HORIZONTAL ADVECTION TERMS AT 500 HPA

Next, we focus on the contribution of the horizontal advection terms at 500 hPa to the propagation of deep cyclones and shallow upper-level cyclones, which are shown in Figure 10 and Figure 11, respectively. For deep cyclones, the instantaneous PV tendency ($\partial q / \partial t$; Fig. 10a) shows a zonal dipolar structure with a slight SW-NE tilt, indicating that at 500 hPa the tendency is for cyclones to move consistently northeastward though the poleward tendency is weaker than at 850 hPa. The zonal advection by the time- and zonal-mean background flow is still responsible for the eastward propagation of cyclones (Fig. 10b). Unlike the situation at 850 hPa, the stationary flow plays a role in advecting cyclones northward at 500 hPa (Fig. 10c). The nonlinear advection term (Fig. 10d) is characterized by a quadrupole structure with stronger magnitude on the northeastern side, but its magnitude is weaker than the advection by the time- and zonal-mean background flow and stationary flow. In summary, the advection by the stationary flow and the nonlinear advection, especially the former one dominates the northeastward propagation of cyclones at 500 hPa.
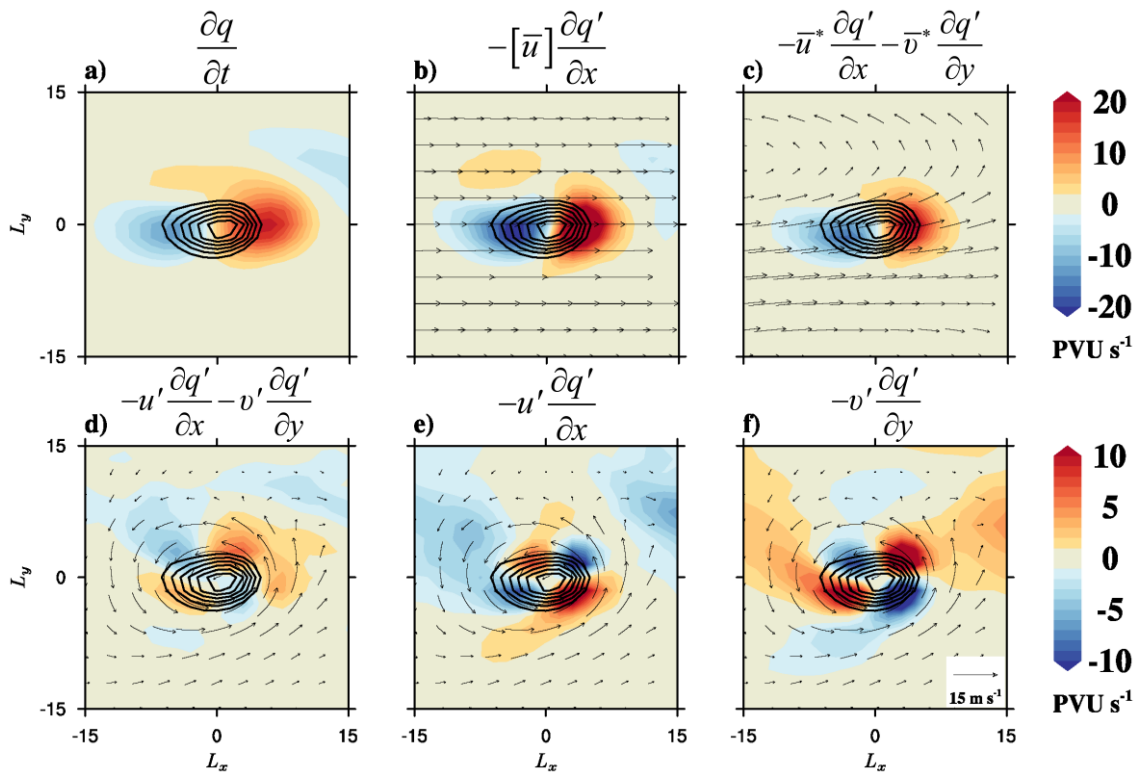

Fig. 10. Same as Fig. 6, but for the 500 hPa PV tendency of deep cyclones. In all panels, the 500 hPa PV anomaly is plotted in black contours, with contour interval of 0.1 PVU (contours are plotted from 0.2 PVU).

24

File generated with AMS Word template 2.0

For shallow upper-level cyclones, the instantaneous PV tendency ($\partial q/\partial t$; Fig. 11a) shows a zonal dipolar structure with a slightly northwest-southeast tilt. The roles of the advection by the time- and zonal-mean background flow (Fig. 11b) and the advection by the stationary flow (Fig. 11c) are similar to that for deep cyclones at 500 hPa, advecting the cyclone eastward and northeastward, respectively. The nonlinear advection term (Fig. 11d) exhibits a dipolar structure in the SW-NE direction and thus contributes to the southward propagation of the PV anomaly. Decomposing the nonlinear advection term into contributions from the zonal and meridional components shows that the meridional nonlinear advection (Fig. 11f) dominates their sum. Therefore, different from deep cyclones, shallow upper-level cyclones move eastward and equatorward, with nonlinear advection as the main process contributing to the meridional movement of extratropical cyclones.
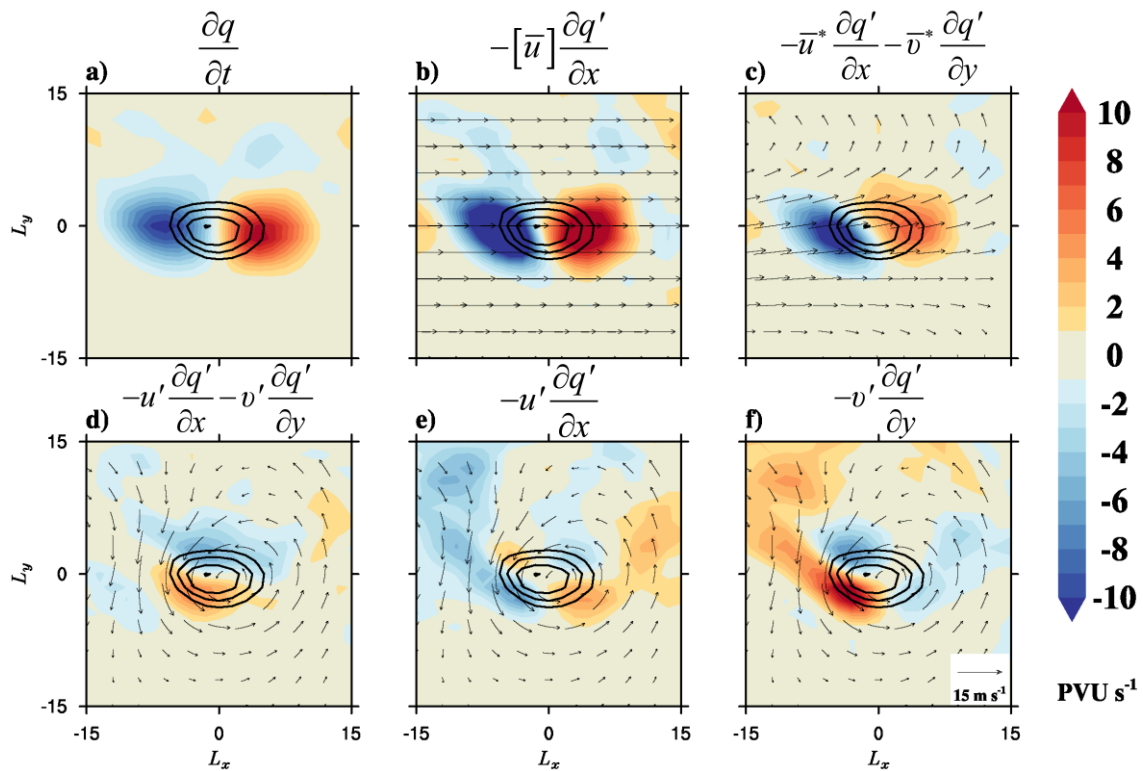

Fig. 11. Same as Fig. 6, but for the 500 hPa PV tendency of shallow upper-level cyclones.

From the above analyses, the horizontal nonlinear advection again plays a different role in the propagation of deep and shallow cyclones at 500 hPa, and especially it may be the dominant mechanism controlling the southward propagation of shallow upper-level cyclones. Therefore, the piecewise PV inversion is similarly applied to decompose the horizontal velocity at 500 hPa. The corresponding nonlinear advection terms are compared to identify

25

File generated with AMS Word template 2.0

the contributions from PV anomalies at different levels. Note that the decomposition of PV anomalies is different here, i.e. $PV'_{1000-700\ hPa}$, $PV'_{600-500\ hPa}$ and $PV'_{400-250\ hPa}$, respectively. As we use the 500 hPa for identifying upper-level cyclones, $PV'_{600-500\ hPa}$ is considered as the anomalies associated with cyclone itself, and the other two are PV anomalies below and above it. The results for deep cyclones and shallow upper-level cyclones are shown in Figure 12 and Figure 13, respectively. For deep cyclones, the sum of the piecewise terms (Figs. 12j-l) is dominated by the nonlinear advection terms induced from the $PV'_{400-250\ hPa}$ (Figs. 12g-i). Though the nonlinear advection by the $PV'_{1000-700\ hPa}$ (Fig. 12a) contributes to southeastward movement, its magnitude is much weaker than that of the $PV'_{400-250\ hPa}$. For shallow upper-level cyclones, contributions from $PV'_{1000-700\ hPa}$ (Fig. 13a) and $PV'_{600-500\ hPa}$ (Fig. 13d) are weak, as there is almost no evident PV anomaly at lower levels as shown in Fig. 5c. The horizontal advection by the wind induced from the $PV'_{400-250\ hPa}$ mainly contributes to the southeastward propagation of cyclones (Fig. 13g). Note that for shallow upper-level cyclones, there is no westward tilt of the low-pressure center and the PV anomaly in vertical as that for deep cyclones (Fig. 5), instead the center of the cyclonic wind induced by the $PV'_{400-250\ hPa}$ is slightly to the east of the 500 hPa PV anomaly, which induces the southward nonlinear advection of the PV anomaly at 500 hPa. Therefore, for both deep and shallow cyclones, the nonlinear advection at 500 hPa is dominated by the wind induced from the $PV'_{400-250\ hPa}$.

26

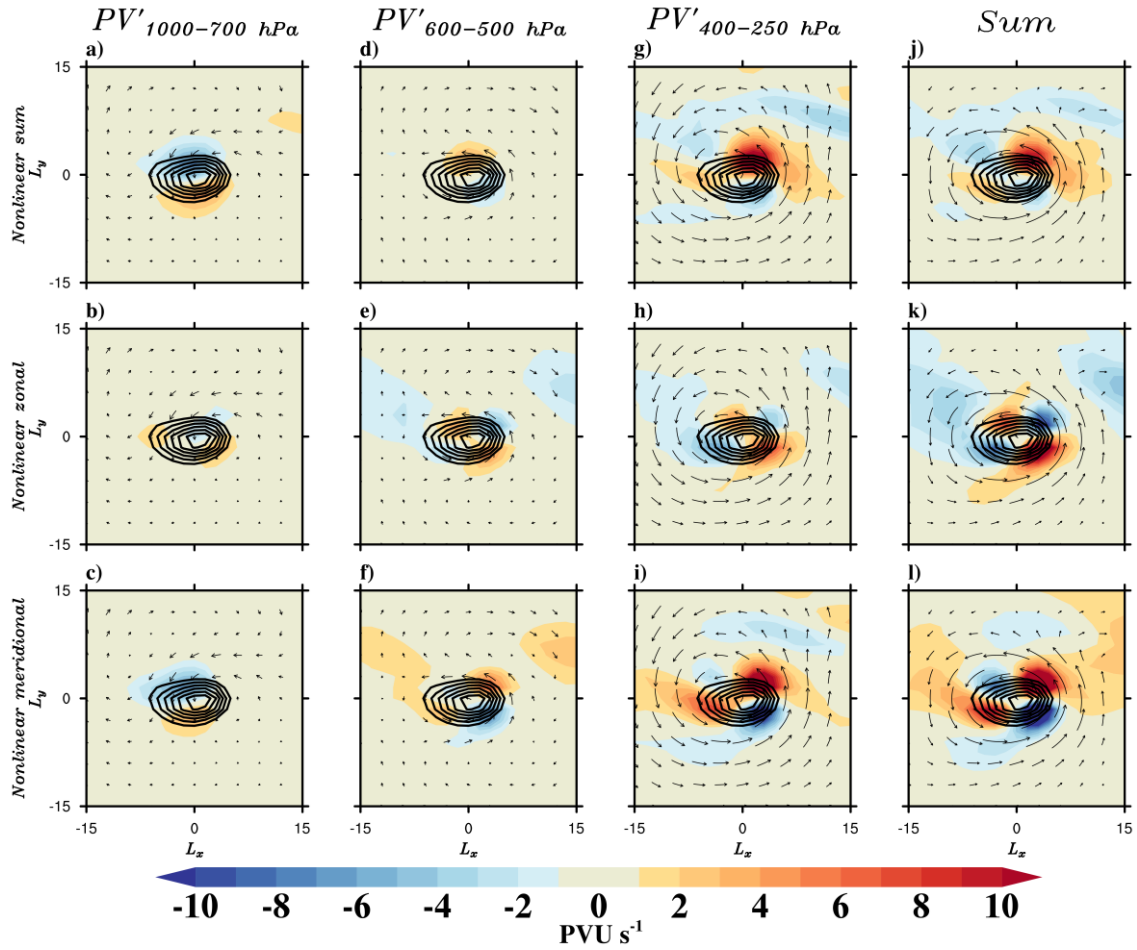File generated with AMS Word template 2.0

Fig. 12. Piecewise PV decomposition of the nonlinear PV advection terms for deep cyclones. Contributions to the PV tendency at 500 hPa from (top)-(bottom) the sum of nonlinear advection terms, the zonal and meridional nonlinear advection. (left)-(right) The contributions to nonlinear PV advection at 500 hPa induced from the PV anomaly at 1000-700 hPa, 600-500 hPa, 400-250 hPa and the sum. All quantities are normalized by 10^{-6} PVU s^{-1}. In each panel the associated winds (black arrows) induced by each of the PV pieces above are also shown. In all panels, the 500 hPa PV anomaly is plotted in black contours, with contour interval of 0.1 PVU (contours are plotted from 0.2 PVU). L_x and L_y denote the relative longitude and latitude extent of the composite box, respectively.
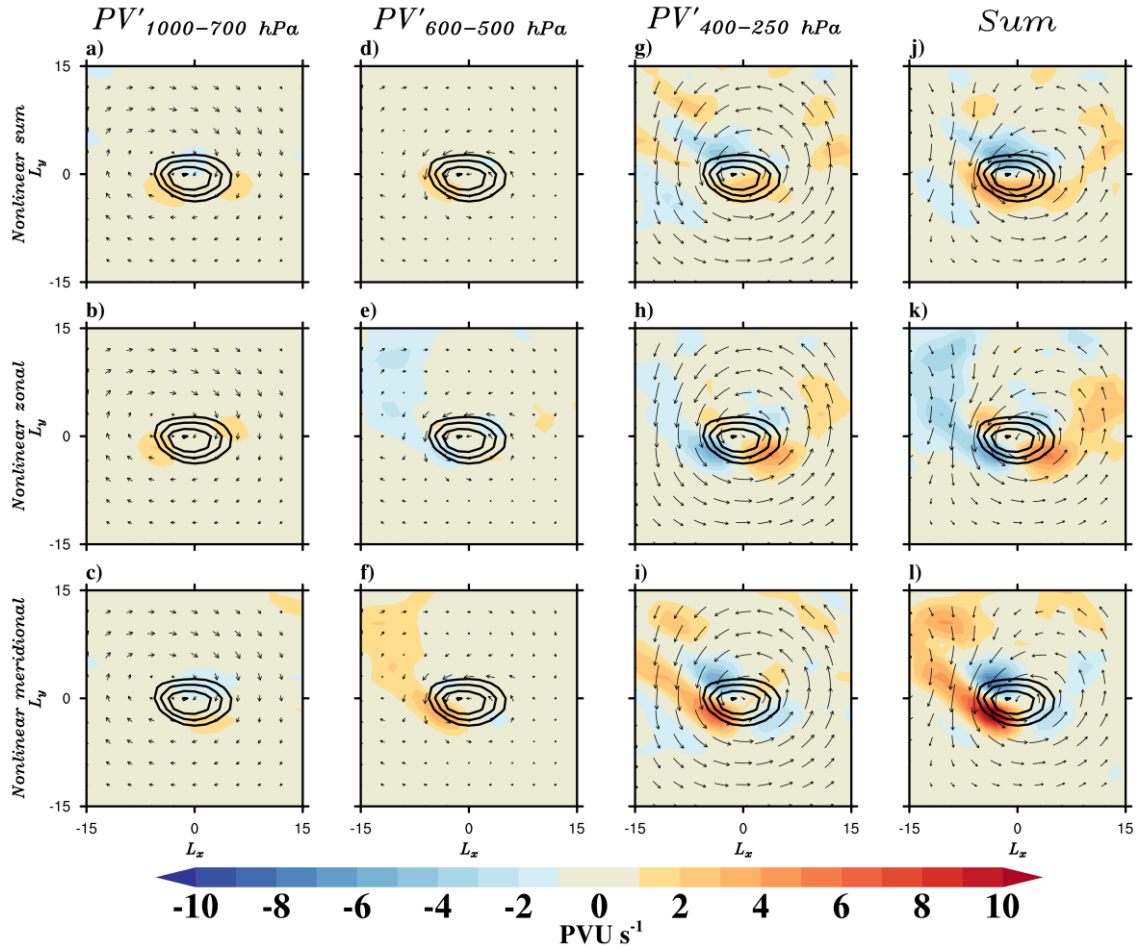
Fig. 13. Same as Fig. 12, but for the shallow upper-level cyclones. In all panels, the 500 hPa PV anomaly is plotted in black contours, with contour interval of 0.1 PVU (contours are plotted from 0.2 PVU).

Please note that in order to test the robustness of the results in Figures 8-9 and 12-13, similar piecewise PV inversions are conducted but decomposing the PV anomaly all into four pieces ($PV'_{1000-925\ hPa}$, $PV'_{850-700\ hPa}$, $PV'_{600-500\ hPa}$ and $PV'_{400-250\ hPa}$). The results are found generally consistent with those presented here (not shown). The conclusions are the same no matter we decompose the PV anomaly into three or four pieces.

b. Diabatic heating and vertical advection

Diabatic processes associated with ETCs are known to play a significant role not only in cyclogenesis (Ahmadi-Givi et al. 2004; Willison et al. 2013) and intensification processes (Büeler and Pfahl 2017; Attinger et al. 2021) but also in the poleward propagation of the low-

28

level cyclones (Coronel et al. 2015; Tamarin and Kaspi 2016, 2017b). Here we further investigate whether the contribution of diabatic heating to the propagation of deep and shallow cyclones is different.

The contribution of the diabatic heating and vertical advection terms to the PV tendency at 850 hPa for deep and shallow low-level cyclones is shown in Figure 14. For deep cyclones, the total diabatic heating term (Fig. 14a) exhibits a dipolar structure with an evident SW-NE tilt and the strongest magnitude among all the terms in the budget. Accordingly, it is the major contributor to the poleward motion of deep cyclones at 850 hPa. While for shallow low-level cyclones, the diabatic heating is characterized by a more zonal dipolar structure (Fig. 14b) and thus only advects cyclones eastward, with little contribution to their poleward propagation. For both deep and shallow cyclones, the LHR at 850 hPa (Figs. 14c and 14d) is the main contributor to the total diabatic heating. The vertical advection term for deep cyclones (Fig. 14e) acts in general to move cyclones southwestward, but with much weaker magnitude. For shallow cyclones (Fig. 14f), the vertical advection term is too weak to play any role for the movement. We have further checked the horizontal distributions of vertical velocity and precipitation in supplemental material (Figure S19). They all exhibit almost the same patterns as their latent heating in Figs. 14c and 14d. Deep cyclones produce rainfall and release latent heat at their northeastern side, while the shallow low-level cyclones produce rainfall and release latent heat over a broader region at their eastern side. Such differences in rainfall distributions account for the different role of the diabatic heating in the latitudinal movement of deep and shallow cyclones.
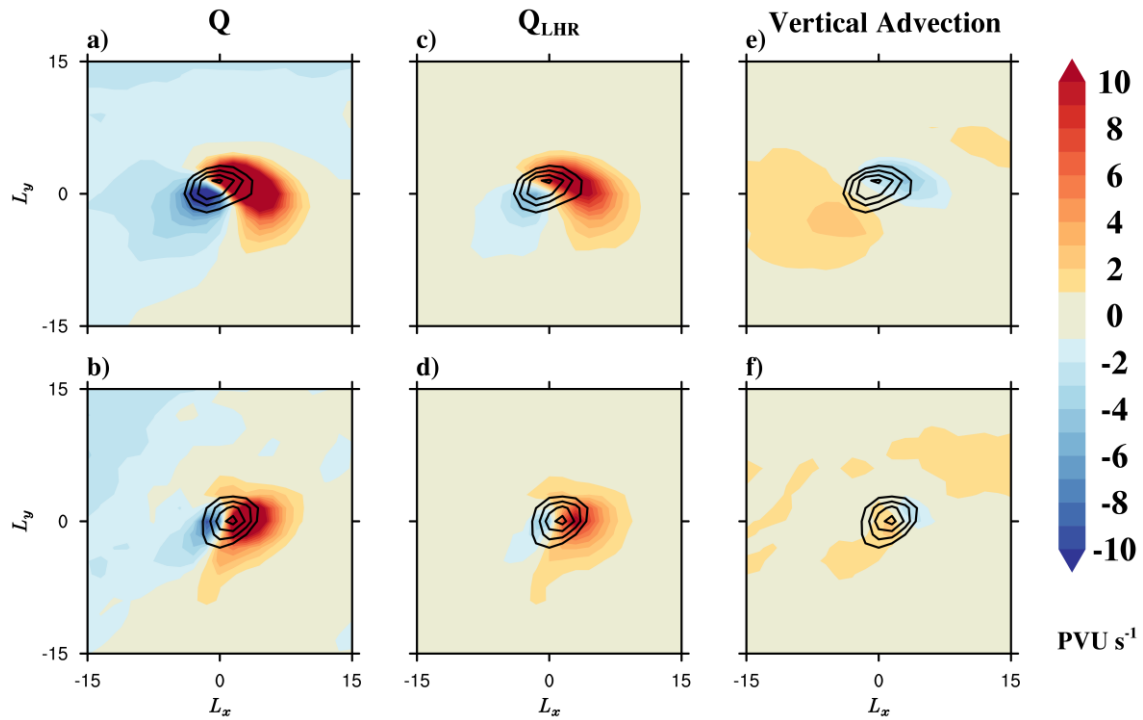
File generated with AMS Word template 2.0

Fig. 14. The 850 hPa PV tendency from (a-b) total diabatic heating (Q), (c-d) diabatic heating associated with the latent heating release (Q_{LHR}) and (e-f) the vertical advection term for deep cyclones (top row) and shallow low-level cyclones (bottom row), respectively. All quantities are normalized by 10^{-6} PVU s^{-1}. In all panels, the 850 hPa PV anomaly is plotted in black contours, with contour interval of 0.1 PVU (contours are plotted from 0.2 PVU). Lx and Ly denote the longitude and latitude extent of the composite box, respectively.

The roles of the diabatic heating and vertical advection at 500 hPa for deep and shallow upper-level cyclones (Fig. 15) are completely different compared to the situation at 850 hPa. For deep cyclones, the total diabatic heating (Fig. 15a) produces an evident negative tendency at the eastern side of the PV anomaly, acting to offset the eastward movement of the cyclone. For shallow upper-level cyclones, the role of diabatic heating becomes much weaker (Fig. 15b), mainly acting to weaken the strength of the cyclone and has little contribution to their movement. At 500 hPa, the contribution of LHR is no longer similar to that of the total diabatic heating for both deep and shallow cyclones. For deep cyclones, the Q_{LHR} produces positive and negative PV tendency on the southwestern and northeastern sides of the PV anomaly, respectively, moving cyclones southwestward (Fig. 15c). For shallow cyclones, the Q_{LHR} makes little contribution to the development and movement of the cyclones (Fig. 15d), consistent with the study of Pepler and Dowdy (2020) showing that shallow upper level cyclones typically produce little precipitation. Different from the situation at 850 hPa, the

30

File generated with AMS Word template 2.0

vertical advection term at 500 hPa (Figs. 15e and 15f) is of the same order of magnitude as the horizontal advection terms, and it plays an important role in hindering the northeastward movement of deep cyclones and the southeastward propagation of shallow upper-level cyclones. In summary, the diabatic heating and vertical advection at 500 hPa are detrimental to both deep and shallow cyclone propagation.
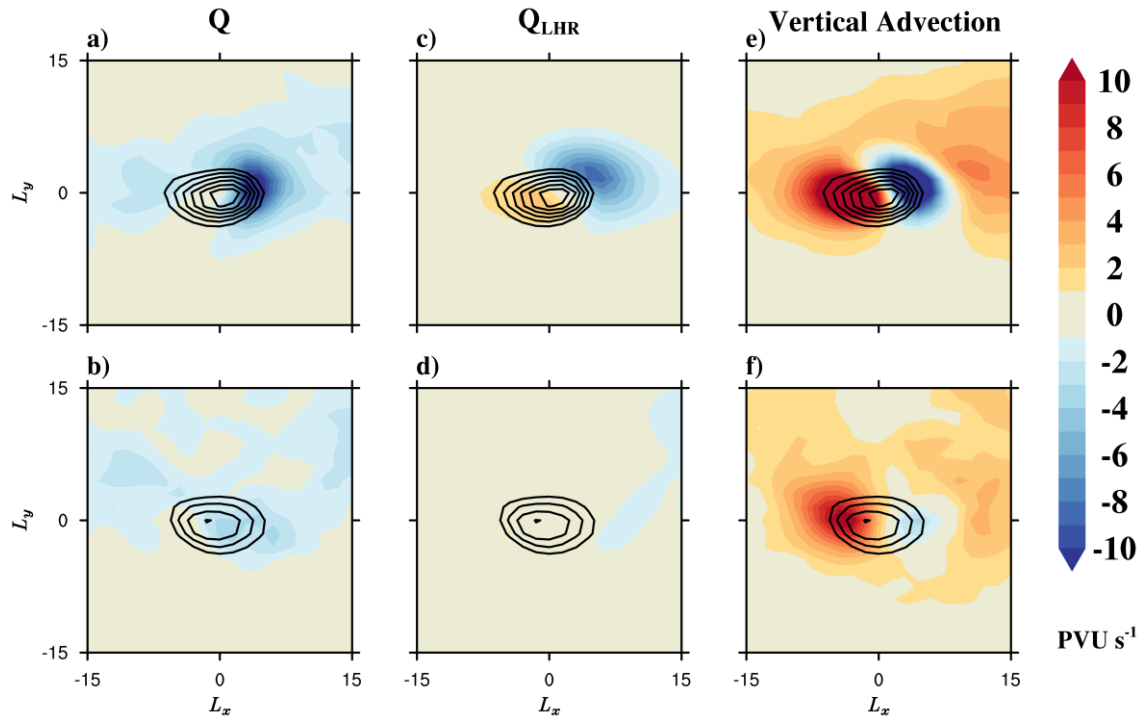

Fig. 15. Same as Fig. 14, but for 500 hPa PV tendency of deep and shallow upper-level cyclones. The 500 hPa PV anomaly is plotted in black contours, with contour interval of 0.1 PVU (contours are plotted from 0.2 PVU).

5. Summary and discussion

The North Pacific is one of the main storm track regions in the Northern Hemisphere, where ETCs are most intense and active, especially in the cold seasons. The movement of NP cyclones identified at a single atmospheric level has been extensively studied (Sickmöller et al. 2000; Mesquita et al. 2010; Tamarin and Kaspi 2017a). In this work, we extend the study to the movement of wintertime North Pacific ETCs by classifying them into deep cyclones, shallow low-level cyclones and shallow upper-level cyclones. By tracking the cyclones at different vertical levels from a Lagrangian PV perspective, we identify different propagation characteristics and mechanisms of deep and shallow ETCs over the North Pacific. Our study

31

File generated with AMS Word template 2.0

shows that shallow low-level cyclones propagate more poleward than deep cyclones, and the shallow upper-level cyclones mainly move eastward and slightly equatorward.

A PV tendency budget analysis is applied to quantify the contributions of dynamic and thermodynamic processes to the different cyclone propagation. Based on the composite analysis of the PV budget, we find that the mechanisms controlling the propagation of the three categories of cyclones are distinct. As suggested by Tamarin and Kaspi (2016), where the PV budget for cyclones identified at lower levels is investigated, the nonlinear advection and diabatic heating are the two main processes contributing to the poleward movement of cyclones. Our results provide additional evidence from a reanalysis that confirms their study. Furthermore, by investigating the PV budget at different levels, we show that the two processes play different roles in deep and shallow cyclones. At the lower level (i.e. 850 hPa), the diabatic heating, which is mostly associated with the latent heat release, is the major contributor to the poleward movement of deep cyclones. However, nonlinear advection has little contribution to their poleward movement and instead slightly hinders their eastward propagation. On the contrary, nonlinear advection terms play a crucial role in advecting shallow low-level cyclones poleward and the diabatic heating terms are mainly responsible for their eastward propagation with little contribution to their poleward movement. At the upper level (i.e. 500 hPa), the diabatic heating diminishes the intensity of shallow upper-level cyclones with little contribution to their movement. This is mainly due to the fact that the diabatic heating creates a positive PV tendency below and a negative PV tendency above the maximum heating around 850 hPa. Deep cyclones move zonally and poleward, which is mainly by the advection by the stationary flow. For shallow upper-level cyclones, nonlinear advection is the only force advecting cyclones equatorward. The different contributions of each budget term for the three categories of cyclones are summarized in Fig. 16.

Piecewise PV inversion analysis is carried out to further understand the different effects of the nonlinear advection term on deep and shallow cyclones. By decomposing the nonlinear advection term into contributions from PV anomalies at different vertical levels, we show that for deep cyclones, the surface and upper-level PV anomalies have comparable but opposite influence on the cyclone propagation. Therefore, the nonlinear advection has a small net contribution to the deep cyclone's meridional movement. For both shallow low-level cyclones and shallow upper-level cyclones, the nonlinear advection by winds induced from the upper tropospheric PV anomaly plays a major role in advecting cyclones poleward and

equatorward, respectively. The different effects of the nonlinear advection on low-level and upper-level shallow cyclones may be related to their different PV anomaly distributions at upper levels (as shown in Fig. 5).
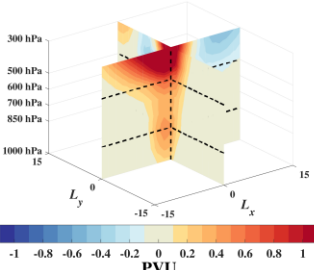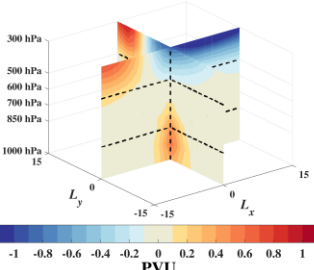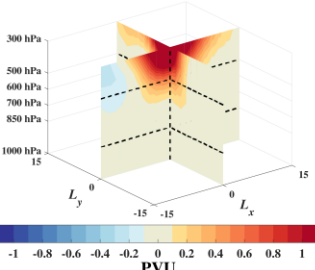
Cyclone Categories	Deep Cyclone	Shallow Low-Level Cyclone	Shallow Upper-Level Cyclone
Vertical Structure			
Movement Direction	Northeastward	Northeastward	Southeastward
$-[\bar{u}]\dfrac{\partial q'}{\partial x}$	Move cyclone eastward		
$-\bar{u}^{*}\dfrac{\partial q'}{\partial x}$ $-\bar{v}^{*}\dfrac{\partial q'}{\partial y}$	Move cyclones eastward at 850 hPa; Move cyclones northeastward at 500 hPa.	Move cyclone eastward	Move cyclone northeastward
$-u'\dfrac{\partial q'}{\partial x}$ $-v'\dfrac{\partial q'}{\partial y}$	Hinder the eastward movement at 850 hPa; A small contribution to the poleward motion at 500 hPa.	**One of the mechanisms controlling poleward movement**	**Key process controlling the southward movement**
$-\omega\dfrac{\partial q}{\partial p}$	Hinder cyclone's movement (magnitude is much stronger at 500 hPa)		
Q	**Move cyclone northeastward at 850 hPa**	Move cyclone eastward	Weaken the strength of the cyclone

Fig. 16. The three-dimensional structure, movement direction and the contributions of each PV budget terms (discussed in the manuscript) to the cyclone movement are shown for three categories of cyclones. The content in bold denotes the key term that contributes to the meridional movement of cyclones.

In this study, we classify the extratropical cyclones into deep and shallow systems, and delineate the different mechanisms for their meridional movement. It has been suggested that deep cyclones often have higher intensities, longer durations, and more severe winds and rainfall than shallow cyclones (Lim and Simmonds 2007; Pepler and Dowdy 2020, 2021), but a cyclone may not always be 'deep' or 'shallow' throughout its lifecycle and there could exist

33

transitions between the two states. For example, numerical studies (Nie et al. 2016; Huang et al. 2020; Nie et al. 2022) showed that eddies can always generate in the lower level near the oceanic frontal zone, but only part of them can develop into upper levels under the appropriate background state (e.g. along the deep jet stream), with the others confined and dissipated in the lower level. Our statistics for deep and shallow low-level cyclones are consistent with those results. However, the key factors for cyclones developing into deep systems and the mechanisms for the propagation of ETCs during such a transition still require further investigations.

In this study, we focus on the wintertime ETCs over the North Pacific, a season in which ETCs in the region are active with strong background circulations. It is possible that in different seasons, the relative contributions of each process to the ETCs' movement are different with different background states. How the mechanisms of ETCs' movement could change in different seasons is a topic that deserves further studies.

Many studies have shown that the storm tracks shift poleward and expand upward under global warming (Yin 2005; Chang et al. 2012; Priestley and Catto 2022). Tamarin and Kaspi (2017a, 2017c) suggest that the poleward shift of storm tracks is essentially the increased latitudinal displacement of low-level cyclones, which is mainly due to the stronger upper-level winds and enhanced atmospheric water vapor (thus enhanced diabatic heating) in a warmer climate. Since the above two processes play different roles in the propagation of deep and shallow cyclones as shown in our study, it motivates further investigation into how the meridional propagation and associated mechanisms of the deep and shallow cyclones may change in global warming scenarios.

The conclusions drawn from our study highlight the need to examine extratropical cyclones over multiple levels. The analyses presented here can be extended to investigate the movement of ETCs over other regions, such as the Eurasian continent where wintertime ETCs are also active with broad weather and climate impacts. Though climatological properties and development processes of Eurasian ETCs have been extensively studied (Basu et al. 2018; Lin et al. 2019), compared to ETCs over the oceans, the vertical structure of the continental ETCs as well as the difference between deep and shallow cyclones still requires systematic analysis. Future investigation will be carried out on this aspect to help further improve the understanding and prediction of Eurasian ETCs.

File generated with AMS Word template 2.0

Data Availability Statement.

The ERA-Interim reanalysis data were downloaded from https://apps.ecmwf.int/datasets/data/interim-full-daily/levtype=pl/, and the code of Kevin Hodges that was used to generate the tracking results is available at gitlab.act.reading.ac.uk/track/track.

File generated with AMS Word template 2.0

REFERENCES

Ahmadi-Givi, F., G. C. Graig, and R. S. Plant, 2004: The dynamics of a midlatitude cyclone with very strong latent-heat release. *Quarterly Journal of the Royal Meteorological Society*, **130,** 295-323, https://doi.org/10.1256/qj.02.226.

Almazroui, M., A. M. Awad, M. N. Islam, and A. K. Al-Khalaf, 2015: A climatological study: wet season cyclone tracks in the East Mediterranean region. *Theoretical and Applied Climatology*, **120,** 351-365, https://doi.org/10.1007/s00704-014-1178-z.

Attinger, R., E. Spreitzer, M. Boettcher, H. Wernli, and H. Joos, 2021: Systematic assessment of the diabatic processes that modify low-level potential vorticity in extratropical cyclones. *Weather Clim. Dynam.*, **2,** 1073-1091, https://doi.org/10.5194/wcd-2-1073-2021.

Barnes, M. A., T. Ndarana, and W. A. Landman, 2021: Cut-off lows in the Southern Hemisphere and their extension to the surface. *Climate Dynamics*, **56,** 3709-3732, https://doi.org/10.1007/s00382-021-05662-7.

Basu, S., X. Zhang, and Z. Wang, 2018: Eurasian winter storm activity at the end of the century: a CMIP5 multi-model ensemble projection. *Earth's Future*, **6,** 61-70, https://doi.org/10.1002/2017ef000670.

Bengtsson, L., K. I. Hodges, and E. Roeckner, 2006: Storm tracks and climate change. *Journal of Climate*, **19,** 3518-3543, https://doi.org/10.1175/jcli3815.1.

Blender, R., K. Fraedrich, and F. Lunkeit, 1997: Identification of cyclone-track regimes in the North Atlantic. *Quarterly Journal of the Royal Meteorological Society*, **123,** 727-741, https://doi.org/10.1002/qj.49712353910.

Bolton, D., 1980: The computation of equivalent potential temperature. *Monthly Weather Review*, **108,** 1046-1053, https://doi.org/10.1175/1520-0493(1980)108<1046:Tcoept>2.0.Co;2.

Büeler, D., and S. Pfahl, 2017: Potential vorticity diagnostics to quantify effects of latent heating in extratropical cyclones. part I: methodology. *Journal of the Atmospheric Sciences*, **74,** 3567-3590, https://doi.org/10.1175/jas-d-17-0041.1.

36

Čampa, J., and H. Wernli, 2012: A PV perspective on the vertical structure of mature midlatitude cyclones in the Northern Hemisphere. *Journal of the Atmospheric Sciences*, **69,** 725-740, https://doi.org/10.1175/jas-d-11-050.1.

Catto, J. L., L. C. Shaffrey, and K. I. Hodges, 2010: Can climate models capture the structure of extratropical cyclones? *Journal of Climate*, **23,** 1621-1635, https://doi.org/10.1175/2009jcli3318.1.

Chang, E. K. M., S. Lee, and K. L. Swanson, 2002: Storm track dynamics. *Journal of Climate*, **15,** 2163-2183, https://doi.org/10.1175/1520-0442(2002)015<02163:Std>2.0.Co;2.

Chang, E. K. M., Y. Guo, and X. Xia, 2012: CMIP5 multimodel ensemble projection of storm track change under global warming. *Journal of Geophysical Research: Atmospheres*, **117,** D23118, https://doi.org/10.1029/2012jd018578.

Charney, J. G., 1955: The use of the primitive equations of motion in numerical prediction. *Tellus A*, **7,** 22-26, https://doi.org/10.1111/j.2153-3490.1955.tb01138.x.

Chen, L., B. Tan, N. G. Kvamstø, and O. M. Johannessen, 2014: Wintertime cyclone/anticyclone activity over China and its relation to upper tropospheric jets. *Tellus A: Dynamic Meteorology and Oceanography*, **66,** https://doi.org/10.3402/tellusa.v66.21889.

Coronel, B., D. Ricard, G. Rivière, and P. Arbogast, 2015: Role of moist processes in the tracks of idealized midlatitude surface cyclones. *Journal of the Atmospheric Sciences*, **72,** 2979-2996, https://doi.org/10.1175/jas-d-14-0337.1.

Côté, H., K. M. Grise, S.-W. Son, R. de Elía, and A. Frigon, 2015: Challenges of tracking extratropical cyclones in regional climate models. *Climate Dynamics*, **44,** 3101-3109, https://doi.org/10.1007/s00382-014-2327-x.

Davies-Jones, R., 2009: On formulas for equivalent potential temperature. *Monthly Weather Review*, **137,** 3137-3148, https://doi.org/10.1175/2009mwr2774.1.

Davis, C. A., 1992: A potential-vorticity diagnosis of the importance of initial structure and condensational heating in observed extratropical cyclogenesis. *Monthly Weather Review*, **120,** 2409-2428, https://doi.org/10.1175/1520-0493(1992)120<2409:Apvdot>2.0.Co;2.

File generated with AMS Word template 2.0

Davis, C. A., and K. A. Emanuel, 1991: Potential vorticity diagnostics of cyclogenesis. *Monthly Weather Review*, **119,** 1929-1953, https://doi.org/10.1175/1520-0493(1991)119<1929:Pvdoc>2.0.Co;2.

Dee, D. P., and Coauthors, 2011: The ERA-Interim reanalysis: configuration and performance of the data assimilation system. *Quarterly Journal of the Royal Meteorological Society*, **137,** 553-597, https://doi.org/10.1002/qj.828.

Dowdy, A. J., and J. L. Catto, 2017: Extreme weather caused by concurrent cyclone, front and thunderstorm occurrences. *Scientific Reports*, **7,** 8, https://doi.org/10.1038/srep40359.

Emanuel, K. A., M. Fantini, and A. J. Thorpe, 1987: Baroclinic instability in an environment of small stability to slantwise moist convection. part I: two-dimensional models. *Journal of Atmospheric Sciences*, **44,** 1559-1573, https://doi.org/10.1175/1520-0469(1987)044<1559:Biiaeo>2.0.Co;2.

Flaounas, E., S. Raveh-Rubin, H. Wernli, P. Drobinski, and S. Bastin, 2015: The dynamical structure of intense Mediterranean cyclones. *Climate Dynamics*, **44,** 2411-2427, https://doi.org/10.1007/s00382-014-2330-2.

Gómara, I., B. Rodríguez-Fonseca, P. Zurita-Gotor, and J. G. Pinto, 2014: On the relation between explosive cyclones affecting Europe and the North Atlantic Oscillation. *Geophysical Research Letters*, **41,** 2182-2190, https://doi.org/10.1002/2014gl059647.

Hersbach, H., and Coauthors, 2020: The ERA5 global reanalysis. *Quarterly Journal of the Royal Meteorological Society*, **146,** 1999-2049, https://doi.org/https://doi.org/10.1002/qj.3803.

Hodges, K. I., 1994: A general method for tracking analysis and its application to meteorological data. *Monthly Weather Review*, **122,** 2573-2586, https://doi.org/10.1175/1520-0493(1994)122<2573:Agmfta>2.0.Co;2.

——, 1995: Feature tracking on the unit sphere. *Monthly Weather Review*, **123,** 3458-3465, https://doi.org/10.1175/1520-0493(1995)123<3458:Ftotus>2.0.Co;2.

——, 1996: Spherical nonparametric estimators applied to the UGAMP model integration for AMIP. *Monthly Weather Review*, **124,** 2914-2932, https://doi.org/10.1175/1520-0493(1996)124<2914:Sneatt>2.0.Co;2.

File generated with AMS Word template 2.0

——, 1999: Adaptive constraints for feature tracking. *Monthly Weather Review*, **127,** 1362-1373, https://doi.org/10.1175/1520-0493(1999)127<1362:Acfft>2.0.Co;2.

Hodges, K. I., R. W. Lee, and L. Bengtsson, 2011: A comparison of extratropical cyclones in recent reanalyses ERA-Interim, NASA MERRA, NCEP CFSR, and JRA-25. *Journal of Climate*, **24,** 4888-4906, https://doi.org/10.1175/2011jcli4097.1.

Hoskins, B. J., and K. I. Hodges, 2002: New perspectives on the Northern Hemisphere winter storm tracks. *Journal of the Atmospheric Sciences*, **59,** 1041-1061, https://doi.org/10.1175/1520-0469(2002)059<1041:Npotnh>2.0.Co;2.

Huang, J., Y. Zhang, X.-Q. Yang, X. Ren, and H. Hu, 2020: Impacts of North Pacific subtropical and subarctic oceanic frontal zones on the wintertime atmospheric large-scale circulations. *Journal of Climate*, **33,** 1897-1914, https://doi.org/10.1175/jcli-d-19-0308.1.

Jiang, L.-Z., S.-M. Fu, J.-H. Sun, R. Fu, W.-L. Li, S.-X. Zhao, and H. Wang, 2022: Surface wind and vertical extent features of the explosive cyclones in the Northern Hemisphere based on the ERA-I reanalysis data. *International Journal of Climatology*, **42,** 993-1014, https://doi.org/https://doi.org/10.1002/joc.7284.

Kang, J. M., and S. W. Son, 2021: Development processes of the explosive cyclones over the Northwest Pacific: potential vorticity tendency inversion. *Journal of the Atmospheric Sciences*, **78,** 1913-1930, https://doi.org/10.1175/jas-d-20-0151.1.

Kang, J. M., J. Lee, S.-W. Son, J. Kim, and D. Chen, 2020: The rapid intensification of East Asian cyclones around the Korean Peninsula and their surface impacts. *Journal of Geophysical Research: Atmospheres*, **125,** e2019JD031632, https://doi.org/10.1029/2019JD031632.

Kelly, K. A., R. J. Small, R. M. Samelson, B. Qiu, T. M. Joyce, Y.-O. Kwon, and M. F. Cronin, 2010: Western boundary currents and frontal air–sea interaction: Gulf Stream and Kuroshio Extension. *Journal of Climate*, **23,** 5644-5667, https://doi.org/10.1175/2010jcli3346.1.

Kim, H.-S., J.-H. Kim, C.-H. Ho, and P.-S. Chu, 2011: Pattern classification of typhoon tracks using the fuzzy c-means clustering method. *Journal of Climate*, **24,** 488-508, https://doi.org/10.1175/2010jcli3751.1.

File generated with AMS Word template 2.0

Kunz, T., K. Fraedrich, and F. Lunkeit, 2009: Synoptic scale wave breaking and its potential to drive NAO-like circulation dipoles: A simplified GCM approach. *Quarterly Journal of the Royal Meteorological Society*, **135,** 1-19, https://doi.org/https://doi.org/10.1002/qj.351.

Kuwano-Yoshida, A., S. Okajima, and H. Nakamura, 2022: Rapid increase of explosive cyclone activity over the midwinter North Pacific in the late 1980s. *Journal of Climate*, **35,** 1113-1133, https://doi.org/10.1175/jcli-d-21-0287.1.

Lakkis, S. G., P. Canziani, A. Yuchechen, L. Rocamora, A. Caferri, K. Hodges, and A. O'Neill, 2019: A 4D feature‐tracking algorithm: A multidimensional view of cyclone systems. *Quarterly Journal of the Royal Meteorological Society*, **145,** 395-417, https://doi.org/10.1002/qj.3436.

Lakkis, S. G., P. O. Canziani, J. O. Rodriguez, A. E. Yuchechen, A. O'Neill, K. H. Albers, and K. Hodges, 2021: Early 21st century cyclone climatology: a 3D perspective.Basic Characterization. *International Journal of Climatology***,** 1-28, https://doi.org/10.1002/joc.7056.

Leckebusch, G. C., and U. Ulbrich, 2004: On the relationship between cyclones and extreme windstorm events over Europe under climate change. *Global and Planetary Change*, **44,** 181-193, https://doi.org/10.1016/j.gloplacha.2004.06.011.

Lim, E. P., and I. Simmonds, 2007: Southern Hemisphere winter extratropical cyclone characteristics and vertical organization observed with the ERA-40 data in 1979-2001. *Journal of Climate*, **20,** 2675-2690, https://doi.org/10.1175/jcli4135.1.

Lin, D., W. Huang, Z. Yang, X. He, T. Qiu, B. Wang, and Jonathon S. Wright, 2019: Impacts of wintertime extratropical cyclones on temperature and precipitation over Northeastern China during 1979-2016. *Journal of Geophysical Research: Atmospheres*, **124,** 1514-1536, https://doi.org/10.1029/2018jd029174.

Ma, X., and Coauthors, 2017: Importance of resolving Kuroshio front and eddy influence in simulating the North Pacific storm track. *Journal of Climate*, **30,** 1861-1880, https://doi.org/10.1175/jcli-d-16-0154.1.

Mendes, D., and M. D. Mendes, 2004: Climatology of cyclones, anticyclones and storm tracks: revision of concepts. *Revista Brasileira de Geofísica*, **22,** 127-134, https://doi.org/10.1590/S0102-261X2004000200003.

40

Mesquita, M. S., D. E. Atkinson, and K. I. Hodges, 2010: Characteristics and variability of storm tracks in the North Pacific, Bering Sea, and Alaska. *Journal of Climate*, **23,** 294-311, https://doi.org/10.1175/2009jcli3019.1.

Neu, U., and Coauthors, 2013: IMILAST: a community effort to intercompare extratropical cyclone detection and tracking algorithms. *Bulletin of the American Meteorological Society*, **94,** 529-547, https://doi.org/10.1175/bams-d-11-00154.1.

Nie, Y., Y. Zhang, G. Chen, and X.-Q. Yang, 2016: Delineating the barotropic and baroclinic mechanisms in the midlatitude eddy-driven jet response to lower-tropospheric thermal forcing. *Journal of the Atmospheric Sciences*, **73,** 429-448, https://doi.org/10.1175/jas-d-15-0090.1.

——, 2022: Quantifying eddy generation and dissipation in the jet response to upper- versus lower-Level thermal forcing. *Journal of the Atmospheric Sciences*, **79,** 2703-2720, https://doi.org/10.1175/jas-d-21-0307.1.

Okajima, S., H. Nakamura, and Y. Kaspi, 2021: Cyclonic and anticyclonic contributions to atmospheric energetics. *Scientific Reports*, **11,** 13202, https://doi.org/10.1038/s41598-021-92548-7.

Pepler, A., and A. Dowdy, 2020: A three-dimensional perspective on extratropical cyclone impacts. *Journal of Climate*, **33,** 5635-5649, https://doi.org/10.1175/jcli-d-19-0445.1.

——, 2021: Fewer deep cyclones projected for the midlatitudes in a warming climate, but with more intense rainfall. *Environmental Research Letters*, **16,** https://doi.org/10.1088/1748-9326/abf528.

Pezza, A. B., and T. Ambrizzi, 2003: Variability of Southern Hemisphere cyclone and anticyclone behavior: further analysis. *Journal of Climate*, **16,** 1075-1083, https://doi.org/10.1175/1520-0442(2003)016<1075:Voshca>2.0.Co;2.

Pezza, A. B., T. Durrant, I. Simmonds, and I. Smith, 2008: Southern Hemisphere synoptic behavior in extreme phases of SAM, ENSO, sea ice extent, and Southern Australia rainfall. *Journal of Climate*, **21,** 5566-5584, https://doi.org/10.1175/2008jcli2128.1.

Pfahl, S., and H. Wernli, 2012: Quantifying the relevance of cyclones for precipitation extremes. *Journal of Climate*, **25,** 6770-6780, https://doi.org/10.1175/jcli-d-11-00705.1.

File generated with AMS Word template 2.0

Pinheiro, H., M. Gan, and K. Hodges, 2021: Structure and evolution of intense austral cut-off lows. *Quarterly Journal of the Royal Meteorological Society*, **147,** 1-20, https://doi.org/https://doi.org/10.1002/qj.3900.

Pook, M. J., J. S. Risbey, and P. C. McIntosh, 2014: A comparative synoptic climatology of cool-season rainfall in major grain-growing regions of southern Australia. *Theoretical and Applied Climatology*, **117,** 521-533, https://doi.org/10.1007/s00704-013-1021-y.

Priestley, M., and J. Catto, 2022: Future changes in the extratropical storm tracks and cyclone intensity, wind speed, and structure. *Weather and Climate Dynamics*, **3,** 337-360, https://doi.org/10.5194/wcd-3-337-2022.

Priestley, M. D. K., D. Ackerley, J. L. Catto, K. I. Hodges, R. E. McDonald, and R. W. Lee, 2020: An overview of the extratropical storm tracks in CMIP6 historical simulations. *Journal of Climate*, **33,** 6315-6343, https://doi.org/10.1175/jcli-d-19-0928.1.

Raible, C. C., 2007: On the relation between extremes of midlatitude cyclones and the atmospheric circulation using ERA40. *Geophysical Research Letters*, **34,** L07703, https://doi.org/10.1029/2006gl029084.

Raible, C. C., P. M. Della-Marta, C. Schwierz, H. Wernli, and R. Blender, 2008: Northern Hemisphere extratropical cyclones: a comparison of detection and tracking methods and different reanalyses. *Monthly Weather Review*, **136,** 880-897, https://doi.org/10.1175/2007mwr2143.1.

Saha, S., and Coauthors, 2010: The NCEP climate forecast system reanalysis. *Bulletin of the American Meteorological Society*, **91,** 1015-1058, https://doi.org/10.1175/2010bams3001.1.

Schemm, S., H. Wernli, and H. Binder, 2021: The storm-track suppression over the western North Pacific from a cyclone life-cycle perspective. *Weather Clim. Dynam.*, **2,** 55-69, https://doi.org/10.5194/wcd-2-55-2021.

Seiler, C., 2019: A climatological assessment of intense extratropical cyclones from the potential vorticity perspective. *Journal of Climate*, **32,** 2369-2380, https://doi.org/10.1175/jcli-d-18-0461.1.

Serreze, M. C., 1995: Climatological aspects of cyclone development and decay in the Arctic. *Atmosphere-Ocean*, **33,** 1-23, https://doi.org/10.1080/07055900.1995.9649522.

42

File generated with AMS Word template 2.0

Sickmöller, M., R. Blender, and K. Fraedrich, 2000: Observed winter cyclone tracks in the northern hemisphere in re-analysed ECMWF data. *Quarterly Journal of the Royal Meteorological Society*, **126,** 591-620, https://doi.org/10.1002/qj.49712656311.

Sinclair, M. R., 1995: A climatology of cyclogenesis for the Southern Hemisphere. *Monthly Weather Review*, **123,** 1601-1619, https://doi.org/10.1175/1520-0493(1995)123<1601:Acocft>2.0.Co;2.

——, 1997: Objective identification of cyclones and their circulation intensity, and climatology. *Weather and Forecasting*, **12,** 595-612, https://doi.org/10.1175/1520-0434(1997)012<0595:Oiocat>2.0.Co;2.

Tamarin, T., and Y. Kaspi, 2016: The poleward motion of extratropical cyclones from a potential vorticity tendency analysis. *Journal of the Atmospheric Sciences*, **73,** 1687-1707, https://doi.org/10.1175/jas-d-15-0168.1.

——, 2017a: Enhanced poleward propagation of storms under climate change. *Nature Geoscience*, **10,** 908-913, https://doi.org/10.1038/s41561-017-0001-8.

——, 2017b: Mechanisms controlling the downstream poleward deflection of midlatitude storm tracks. *Journal of the Atmospheric Sciences*, **74,** 553-572, https://doi.org/10.1175/jas-d-16-0122.1.

——, 2017c: The poleward shift of storm tracks under global warming: A Lagrangian perspective. *Geophysical Research Letters*, **44,** 10666-10674, https://doi.org/10.1002/2017gl073633.

Wernli, H., and C. Schwierz, 2006: Surface cyclones in the ERA-40 dataset (1958-2001). Part I: Novel identification method and global climatology. *Journal of the Atmospheric Sciences*, **63,** 2486-2507, https://doi.org/10.1175/jas3766.1.

Willison, J., W. A. Robinson, and G. M. Lackmann, 2013: The importance of resolving mesoscale latent heating in the North Atlantic storm track. *Journal of the Atmospheric Sciences*, **70,** 2234-2250, https://doi.org/10.1175/jas-d-12-0226.1.

Woollings, T., B. Hoskins, M. Blackburn, and P. Berrisford, 2008: A new Rossby wave–breaking interpretation of the North Atlantic Oscillation. *Journal of the Atmospheric Sciences*, **65,** https://doi.org/10.1175/2007JAS2347.1.

File generated with AMS Word template 2.0

Yin, J. H., 2005: A consistent poleward shift of the storm tracks in simulations of 21st century climate. *Geophysical Research Letters*, **32,** L18701, https://doi.org/10.1029/2005gl023684.

Zappa, G., L. C. Shaffrey, and K. I. Hodges, 2013: The ability of CMIP5 models to simulate North Atlantic extratropical cyclones. *Journal of Climate*, **26,** 5379-5396, https://doi.org/10.1175/jcli-d-12-00501.1.

Zhang, X. D., J. E. Walsh, J. Zhang, U. S. Bhatt, and M. Ikeda, 2004: Climatology and interannual variability of arctic cyclone activity: 1948-2002. *Journal of Climate*, **17,** 2300-2317, https://doi.org/10.1175/1520-0442(2004)017<2300:Caivoa>2.0.Co;2.

Zhang, Y., Y. Ding, and Q. Li, 2012: A climatology of extratropical cyclones over East Asia during 1958–2001. *Acta Meteorologica Sinica*, **26,** 261-277, https://doi.org/10.1007/s13351-012-0301-2.

File generated with AMS Word template 2.0